Assessment and optimization of double CT bridge girder sections with longitudinal precast decks

Final Project Report

06/30/2022

Andrew Schanck EI, PhD
Research Engineer, University of Maine Civil Engineering

Anthony Diba
Design Engineer, AIT Bridges

William Davids, PhD, PE
Bodwell University Distinguished Professor of Civil and Environmental Engineering, University of Maine

Advanced Structures and Composites Center
35 Flagstaff Rd
University of Maine
Orono, ME 04469

Telephone: 207-581-2123
FAX: 207-581-2074
composites@maine.edu
www.composites.umaine.edu

ACKNOWLEDGEMENTS

Support for this research was provided by the Transportation Infrastructure Durability Center (TIDC) at the University of Maine under grant 69A3551847101 from the U.S. Department of Transportation's University Transportation Centers Program. Additional financial and logistical support was provided by AIT Bridges, whose assistance with specimen manufacturing is greatly appreciated. The results and opinions reported here are solely those of the authors and do not constitute a design guide or specification.

DISCLAIMER

Table of Contents

Index of Figures

Index of Tables

1 Introduction

Durable, reliable infrastructure is paramount to local, state, and national economic growth and development. As these economies continue to grow, so too do the demands placed on existing infrastructure, notably on roads and bridges. To keep up with the ever-increasing demand, new, durable, rapidly erected bridges are needed and in turn require the use of new materials and construction techniques to supersede more conventional, less durable designs. To respond to this need, the University of Maine developed a novel, fiber reinforced polymer (FRP) tub girder (referred to as a "CT girder") for use in new bridge construction as an alternative to conventional steel and prestressed concrete structural members. CT girders have been identified as a promising technology to support sustainable and durable infrastructure development, as they are comparatively light and overcome many of the challenges associated with precast NEXT beam concrete structures by reducing shipping costs and camber variability caused by prestressing. To improve on this system, AIT Bridges, the firm that designs and manufactures FRP bridges and bridge components, and to whom the University of Maine licenses the CT girder system, has proposed connecting two CT girders with a partial precast concrete deck into a new, composite section. This new composite section, as shown in Figure 1, mimics precast double T sections with the aim of expediting and simplifying the transport and construction process over single CT girders with full cast-in-place decks.

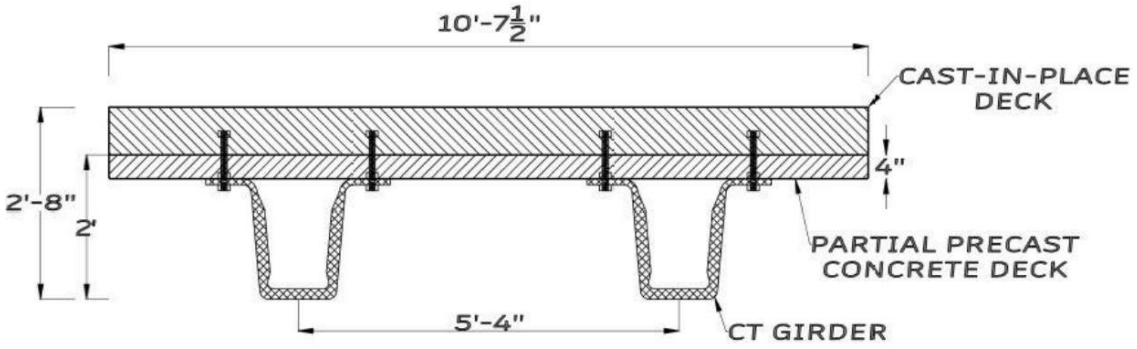

Figure 1: Cross-Sectional View of a Double CT Girder Section

Due to the novelty of the CT girder system, only a small number of research projects and large-scale structural tests have been conducted to assess the girder performance and to date all have focused on the single CT girder with a full-depth CIP deck or pre-cast deck panels. Further, creep behavior of the CT girder has not yet been assessed, and the deck-to-girder shear connection system is also under development. In response, a series of research tasks is underway which aims to assess the performance of the double CT girder's novel girder-deck shear connection, its short-to-medium term creep deflection, and its flexural response under pre-composite service flexural loading and post-composite ultimate flexural loading.

This report is organized into four sections including this introductory section and three subsequent sections describing the background, testing details, and major conclusions drawn in this work. These are:

- Section 2: FRP-concrete ridged shear connection fatigue and ultimate strength testing
- Section 3: Full-scale double CT-girder creep deflection testing
- Section 4: Full-scale double CT-girder service-level and strength testing

Relevant calculations and external contractor's reports are provided in appendices, which are preceded by a short list of references.

2 Ridged FRP-Concrete Shear Connection

2.1 Introduction

To maintain composite action between the girder and partial precast deck, the double CT girder uses a novel shear connection developed previously by the University of Maine [1, 2]. This connection system, seen in Figure 2, uses sinusoidal ridges cast into the girder's FRP upper flanges, which are copied into the deck as it is poured. These interlocking ridges provide a continuous shear key between the components, with uplift forces resisted by discrete shear connectors (similar to shear studs in conventional steel-concrete composite construction or to the reinforcement protruding from prestressed girders and cast into the deck). This connection has been investigated in the past with promising results [1-3] prompting additional investigation and development. In this portion of the project, focus was placed upon the elements providing clamping force rather than the FRP-concrete connection itself. Specifically, FRP threaded rods are investigated as possible clamping elements and stainless steel rods are reevaluated. These elements have the potential to provide adequate clamping load to the connection, while also reducing or eliminating the effects of corrosion inherent when using mild or carbon steel components. Elimination of corrosion damage can potentially improve a structure's overall durability and greatly reduce maintenance demands.

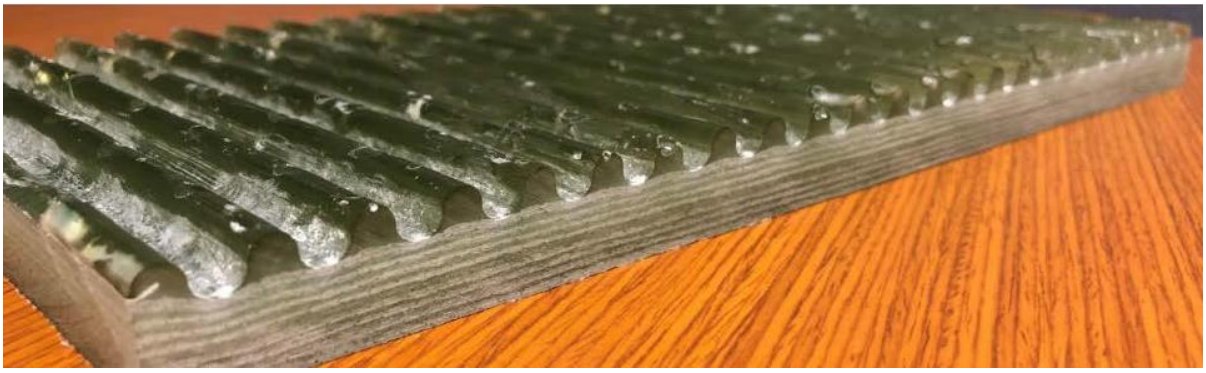

Figure 2: Ridged FRP Shear Connection

2.2 Specimen Fabrication and Details

A total of five shear push-out specimens were cast for testing under fatigue and/or strength-level loading. These were initially divided into two types, each designed to test a different alteration to the original ridged shear connector concept. Three specimens, Specimens 1, 2, and 5, were planned to be cast to test the use of 1 1/8" diameter, non-pretensioned FRP threaded rods to apply clamping force to the connection. The rods, furnished by GBolt to AIT Manufacturing, are characterized by their light weight and high tensile strength. FRP Nuts were used to clamp together the FRP plates and concrete, but, in contrast to previous studies [1-3], were only tightened hand-tight, as opposed to being tightened to a specific pretensioning torque. These specimens were additionally designed to emulate a precast concrete deck connection, as would be present on a double-T CT girder bridge. As such, they were cast by American Concrete Industries (ACInd), a local precaster, using a high early strength concrete mix. Photos of Specimens 1 and 2 can be seen in Figure 3.

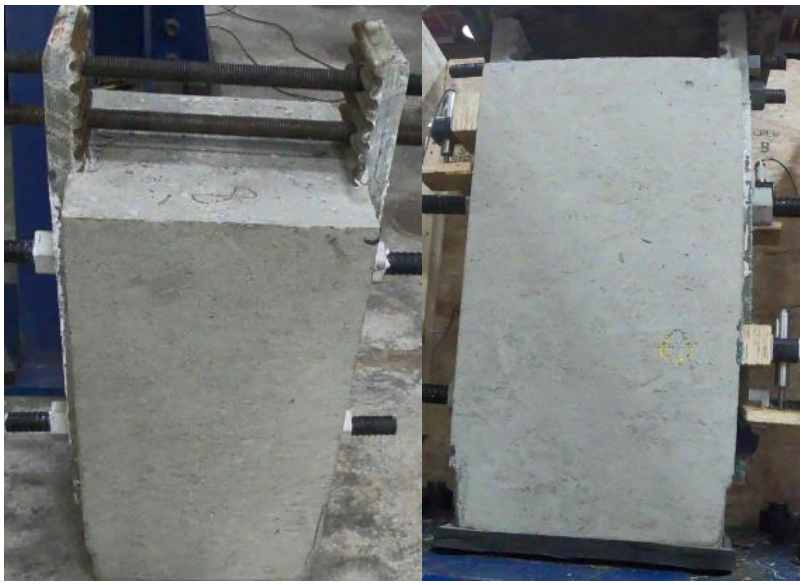

Figure 3: Precast, FRP Rod Specimens (from left to right: Specimen 1, 2)

Late in the testing regime, it was decided by AIT to amend the original design of the third specimen of the first group of specimens (Specimen 5). Rather than using straight, 1 1/8" GBolt studs, this specimen used hooked, 1" diameter GBolts as uplift studs. Additionally, the as-manufactured FRP ridges on the FRP plates were shaved down from their original ½" depth to ¼" to simulate poor manufacturing quality and inform future quality control/quality assurance procedure. This specimen is pictured in Figure 4. Although the changes made to this specimen are worthy of future investigation, they presented significant challenges in the present study. The changes made to Specimen 5 were not initially communicated to the UMaine researchers, who assumed that it would be similar to the previous two (Specimens 1 and 2) and so planned to use

Specimen 5 as a non-fatigue-tested control specimen for assessment of strength or stiffness degradation due to fatiguing. It was not until after having tested Specimen 5 to failure that the changes were communicated. Therefore, conclusions regarding fatigue degradation cannot be readily made for the unaltered specimens, and only limited conclusions can be drawn from the results of tests performed on Specimen 5.

Figure 4: Specimen 5

The remaining two specimens (Specimens 3 and 4) were cast to emulate the potential connection details of a small, single or double CT girder bridge with a cast-in-place deck. These specimens used relatively small diameter (1 in. and ¾ in. for Specimens 3 and 4, respectively), non-pretensioned 18-8 stainless steel rods with end nuts to apply clamping. To emulate the properties of a cast-in-place deck, concrete was cast concurrently with the deck of an actual, single CT girder bridge, the Hampden Grist-Mill Bridge (HGMB) in Hampden, Maine, with concrete from the same batch. This concrete mix was more conventional than the concrete from which the other three specimens were cast, having a lower (4,000 psi) design compressive strength and less-than-ideal curing conditions. It should be noted that, as the bridge's deck was cast in early December, admixtures were included to account for cold-weather curing. These specimens can be seen in Figure 5.

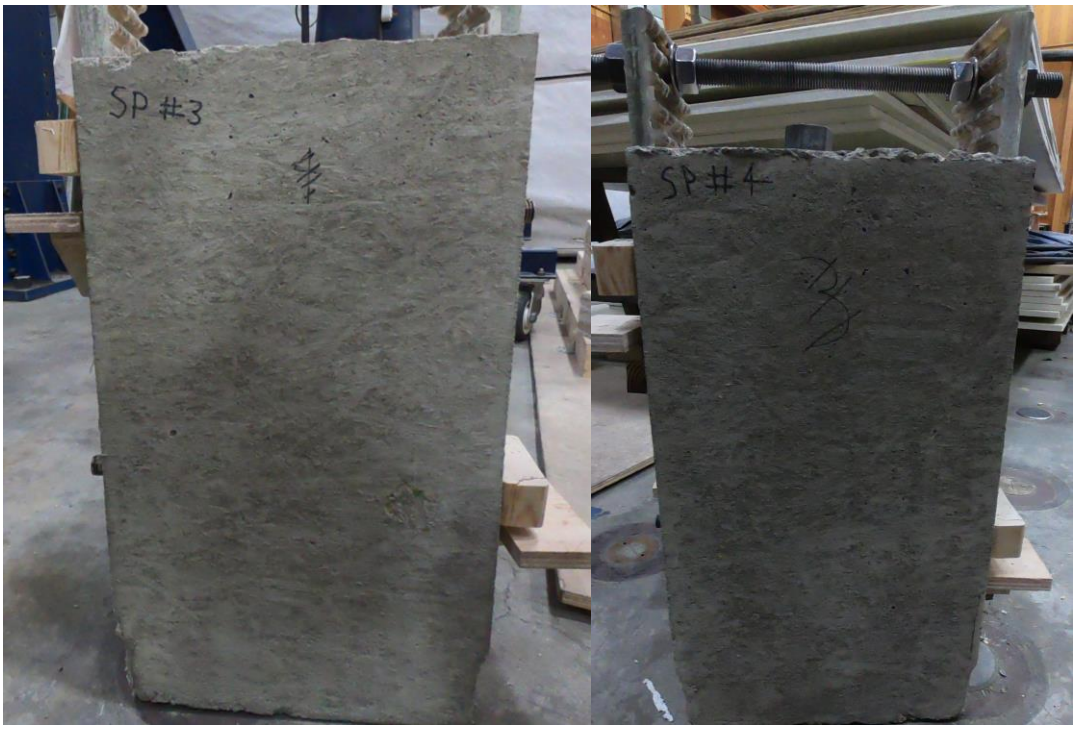

Figure 5: Cast-in-Place, Stainless Steel Rod Specimens (from left to right: Specimen 3, 4)

2.3 Fatigue Tests

Of the five specimens cast and tested, four were tested under AASHTO Fatigue I loading to assess the connection's long-term durability and ability to withstand repeated cyclic loading without significant reduction in performance. Because the ridged FRP-concrete connection had already been evaluated under high fatigue-load [1-3], the tests were conducted to investigate the feasibility of non-pretensioned FRP and stainless steel shear studs as a replacement for the pretensioned Grade 5 bolts used in the previous studies. Each of the tested specimens was subjected to 6 million load cycles, with a load range designed to produce shear flow between FRP and concrete, matching that of dead and factored Fatigue I loading on a proposed double CT-girder bridge. These loading calculations can be found in Appendix A1.

2.3.1 Protocol and Instrumentation

The fatigue specimens were loaded to mimic the American Association of State Highway and Transportation Officials (AASHTO) Fatigue I shear flow (0.92 kip/in) predicted for a representative 53-foot, simply-supported double CT girder bridge with precast deck [4]. These specimens were subjected to a load range of 42.0 kips (29.0 kips minimum, 71.0 kips maximum) as calculated in Appendix A1. Before beginning a test, the strength of the concrete making up each specimen was determined by subjecting cylinder specimens (cast at the time of the specimens) to uniaxial compression according to ASTM C39 [5]. The cylinders corresponding to the specimens cast by ACInd (Specimens 1 and 2) were tested using a Forney F-325EX-B-CPILOT compression-testing machine, and the cylinders corresponding to the specimens cast concurrently with the deck

of the HGMB (Specimens 3 and 4) were tested as part of the bridge's quality assurance procedures by S.W. Cole Engineering (with test reports provided in Appendix A2). Table 1 presents the average experimentally determined concrete strength at the onset of fatigue testing for each fatigue specimen.

Table 1: Push-Out Specimen Concrete Compressive Strength at Start of Fatigue Testing

Specimen	Date of Cylinder Tests	f'_c (psi)	Shear Connector
1	9/22/2020	10,600	FRP
2	10/20/2020	11,000	FRP
3	1/5/2021	6,670	1" Stainless Rod
4	1/5/2020	6,670	¾" Stainless Rod

To estimate damage incurred over the course of testing, the accumulated slip between the concrete blocks and GFRP plates for each fatigue-loaded specimen was measured continuously using four, ±0.2 in. linear variable differential transformers (LVDTs). These LVDTs were mounted adjacent to each of the two studs in each of the two GFRP plates on either side of each specimen. The LVDTs recorded the relative displacement between concrete and GFRP continuously over the course of a test at a sampling rate of 100 Hz. The accumulated slip between components could therefore be calculated over the test as the measured relative displacement less the relative displacement at the beginning of the test. Cyclic forces were applied at 3 Hz by an Instron 110 kip servo-hydraulic actuator running in load control.

2.3.2 Results

2.3.2.1 Specimen 1

Fatigue testing of specimen 1 began on September 22, 2020 and 6 million load cycles were applied without failure. Figure 6 presents the apparent slips recorded over the course of testing. A few observations can be made from these recorded data. First, the maximum recorded slips are of similar magnitude to those recorded in the previous study [1, 3] for fatigue specimens using pretensioned 18-8 stainless steel rods to maintain clamping between concrete and FRP. However, in these previous tests smaller fatigue loads were applied, suggesting that these FRP rods may be adequate in this application. However, the FRP rod recorded slips are larger than the slips recorded for specimens in [1, 3] that used pretensioned Grade 5 bolts to apply clamping force under slightly higher loads. A second observation is that, from the positive slope of the slips recorded at the tops of the FRP plates, it appears that the repeated loading caused some cumulative damage of either the concrete, FRP plates, FRP rods, or some combination which increased over time. Finally, it can be seen that the slips recorded at the top of the plates were much higher than those recorded at the bottoms. Although it is possible that the tops slipped much more than the bottom, it should be

noted that during testing, it was observed that the applied load tended to cause bowing in the top portions of the FRP plates from lack of lateral support. This movement may have been detected by the LVDTs and was thus mistakenly interpreted as relative slip.

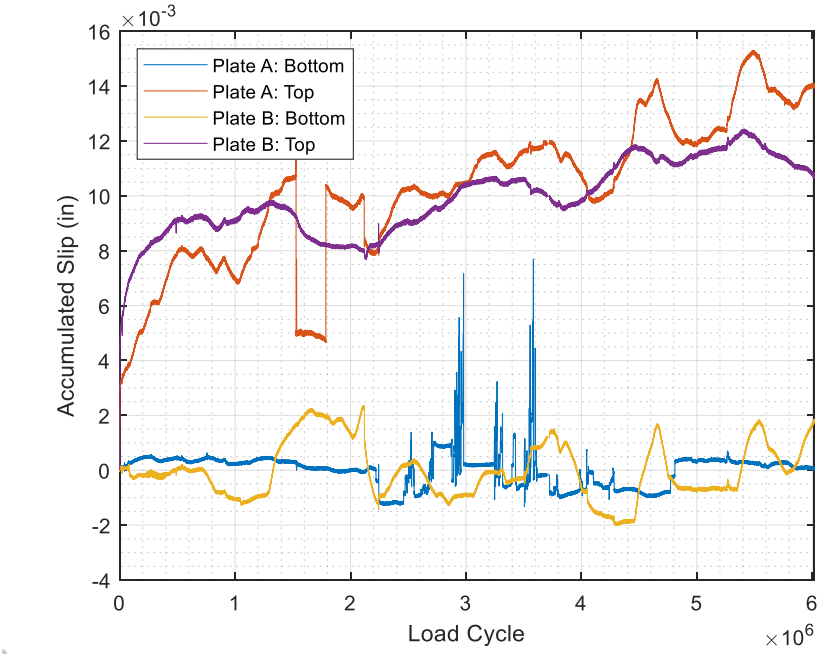

Figure 6: Specimen 1 - Apparent Slip Accumulated over Fatigue Testing

To identify possible damage to, or loss of load-slip performance in Specimen 1 over the course of testing, its recorded slips were averaged across the four LVDTs at the beginning and end of testing and plotted. Figure 7 shows the averaged slip measured over the course of the one-thousandth and six-millionth load-cycles. As can be seen, the average load-slip response increased somewhat throughout the test. This is likely a combination of the increase in slip identified previously, and minor damage accumulated over the test. Regardless, the shape remained constant from the beginning to end of the test. The response to loading and unloading is about the same, with little increase in hysteresis after 6,000,000 cycles.

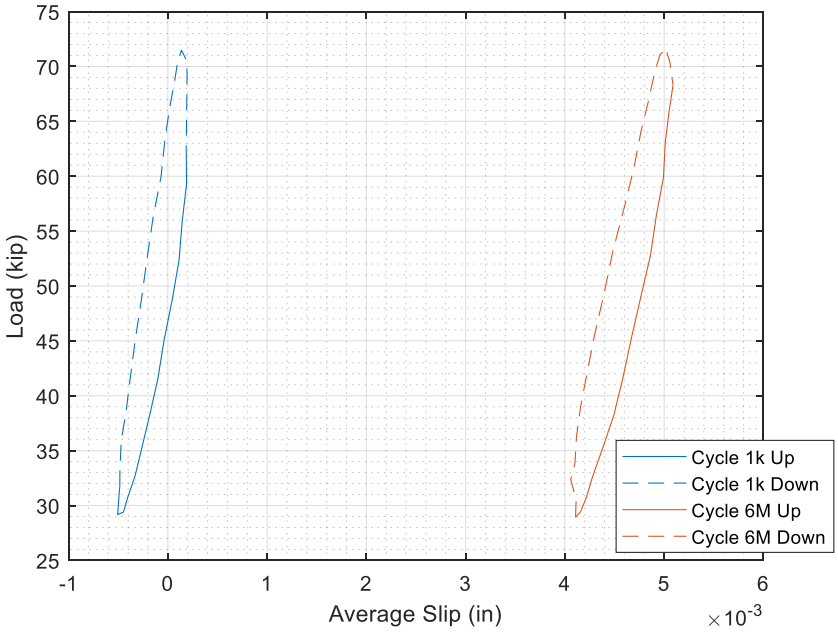

Figure 7: Specimen 1 – Average Load-Slip Behavior at Beginning and End of Fatigue Testing

2.3.2.2 Specimen 2

Fatigue testing of specimen 2, which duplicated the materials and geometry of Specimen 1, began on October 19, 2020 and the specimen withstood 6 million load cycles without failure. To prevent the bowing effect observed at the top of the plates on Specimen 1, two sets of threaded rod were inserted into the holes at the top of the FRP plates, with a nut and washer on either side of each plate. Figure 8 presents the apparent slips recorded over the course of testing. As is immediately apparent, from the onset of fatigue loading, the LVDT at the bottom of Plate B recorded apparent slips that were exceptionally high relative to the other LVDTs and relative to Specimen 1. Upon inspection of the specimen, it was discovered that the FRP nut closest to this LVDT had a crack extending from the outer surface to the inner thread as seen in Figure 9. It is unknown if the crack developed during specimen assembly or during the curing of the structural adhesive applied to prevent nut loosening. In either case, the crack may have limited the amount of clamping force the nut applied to the panel, thereby causing more slip. It can also be seen in Figure 8 that the slips recorded by the other LVDTs were smaller than those recorded at the top of Specimen 1, and similar to those recorded in previous tests [1, 3]. This suggests that the additional hardware provided at the plate tops prevented the bowing behavior observed from Specimen 1, reducing the amount of non-slip movement to be recorded and falsely interpreted as slip.

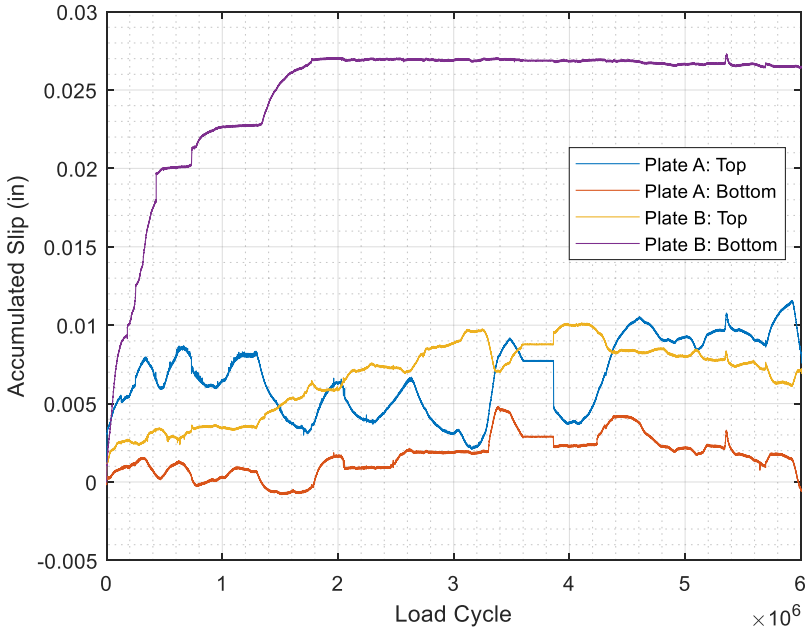

Figure 8: Specimen 2 - Apparent Slip Accumulated over Fatigue Testing

Figure 9: Specimen 2 – Crack in Plate B, Bottom FRP Nut

The average load-slip behavior of Specimen 2 was again extracted to track any changes in behavior over the course of fatigue cycling. The behavior was identified twice; once in Figure 10 with the data from the bottom of Plate B included, and once in Figure 11 with these data omitted. Both Figure 10 and 11 show that Specimen 2 experienced some loss of stiffness between the beginning and end of the test, observable as a slight rotation of the load-unload path between the one-thousandth and six-millionth load-cycles. This indicates that the specimen underwent a small amount of damage, resulting in a loss of stiffness. This may be due to the reduced participation by

the bottom part of Plate B to slip resistance caused by reduced clamping force. However, minimal hysteretic response (seen as an increase in recorded slip during loading relative to unloading) was recorded.

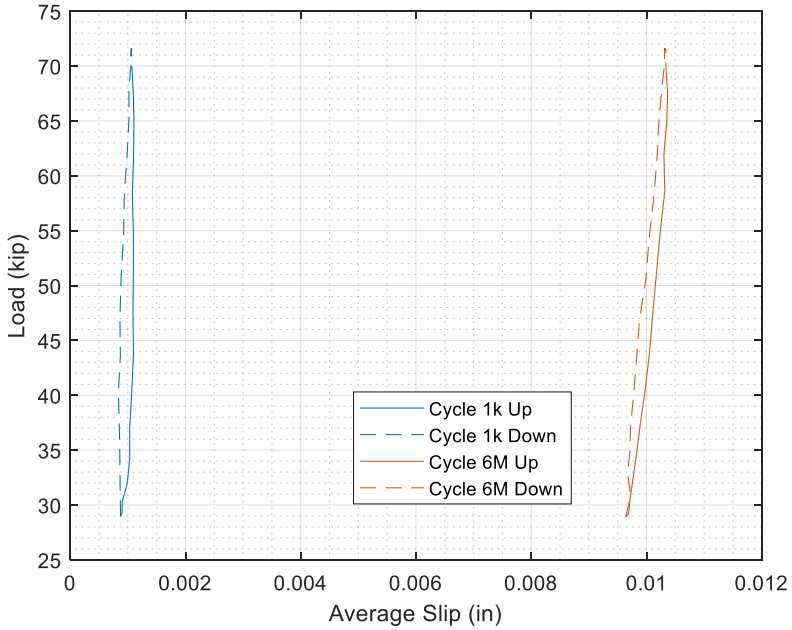

Figure 10: Specimen 2 – Average Load-Slip Behavior at Beginning and End of Fatigue Testing – Cracked Nut Data Included

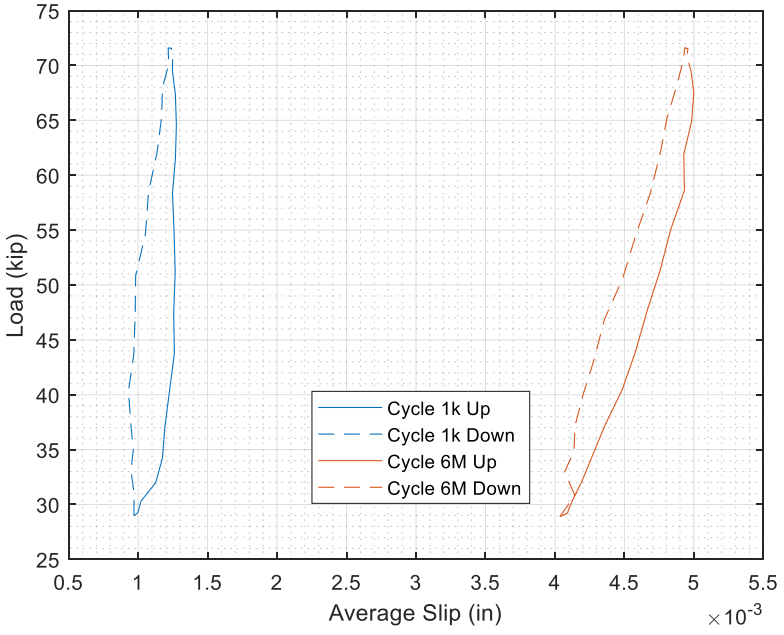

Figure 11: Specimen 2 – Average Load-Slip Behavior at Beginning and End of Fatigue Testing – Cracked Nut Data Omitted

2.3.2.3 Specimen 3

Specimen 3 began fatigue testing on December 18, 2020 and was able to withstand 6 million load cycles without failure. The accumulated slip recorded during this test by all LVDTs was dominated by a large initial slip (0.015 in – 0.029 in.) accumulated within the first 750,000 load cycles with a much less drastic accumulation thereafter. This can be seen in Figure 12, which presents the apparent slips recorded over the course of testing. Inspection of the specimen after fatiguing did not reveal an apparent source of this large, initial slip. However, the differences between this specimen and the previous two may reveal some possibilities. First, at the onset of testing the concrete comprising the specimen was relatively young, being cast only 10 days prior. Assuming that concrete reaches its "full" cure at 28 days, the specimen had not fully cured until it had been subjected to more than 4 million load cycles. Therefore, this large, initial slip may have been a function of the concrete's immaturity leading to reduced stiffness. This is further evidenced by the fact that, as seen later, Specimen 4 did not exhibit this large accumulation of slip at the onset of fatiguing, despite using identical concrete cast at the same time and using smaller shear connectors to apply clamping load. It should also be noted that, after the large, initial accumulation, the specimen's recorded slip seemed to stabilize until around 1,800,000 load-cycles, after which slip decreased rapidly, was regained, and then increased gradually for the remainder of testing. This may indicate the onset, and then development of minor damage to the connection.

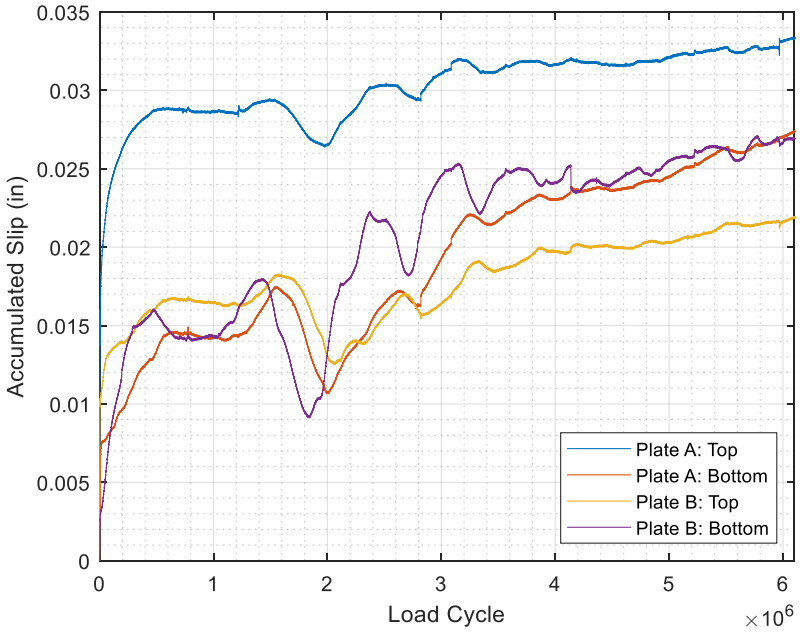

Figure 12: Specimen 3 - Apparent Slip Accumulated over Fatigue Testing

As in the previous specimens, the average load-slip behavior of Specimen 3 was extracted to track any changes in behavior over the course of fatigue cycling. This is presented in Figure 13. As expected, the average slip through the entire load range increased significantly over the course of fatiguing, due mostly to the large increase in slip recorded during the first 750,000 load-cycles.

This can be seen as the large shift in the specimen's load-slip response between 1,000 and 1,000,000 cycles, which has been included here as well. Additionally, the difference between slips at maximum and minimum load increased by a small amount, visible as a clockwise rotation of the load-slip curve and indicating a small decrease in stiffness. Finally, very little load-unload hysteresis was accumulated, as indicated by an insignificant widening of the space between loading and unloading curves at the one-thousandth and six-millionth load-cycles. These factors combine to indicate that only a small degree of damage was incurred over the course of fatiguing.

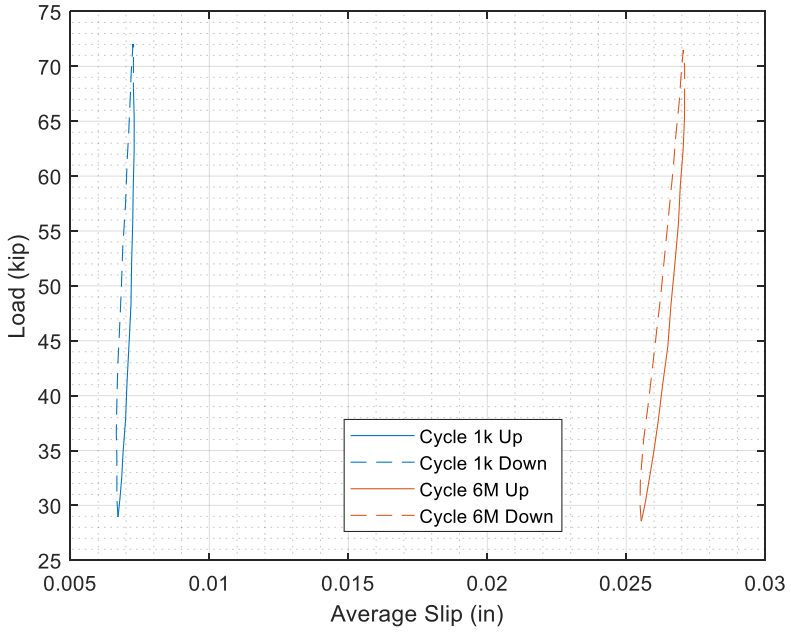

Figure 13: Specimen 3 – Average Load-Slip Behavior at Beginning and End of Fatigue Testing

2.3.2.4 Specimen 4

Specimen 4 began fatigue testing on January 12, 2021 and withstood the full 6 million load-cycles without failure. As seen in Figure 14, accumulated slip was initially relatively small, remaining less than 0.01 in. until around 1,800,000 load cycles. At around 1,300,000 cycles, the slips recorded at the bottom of Plate A and throughout Plate B increased rapidly, stabilizing at around 3,500,000 cycles. Notably however, the slip recorded at the top of Plate A did not display this behavior, remaining stable until around 1,700,000 cycles when it began to decrease gradually, finishing with a small net-negative accumulated slip. This behavior indicates a smaller movement of the plate at this location relative to the concrete after being fatigued than at the onset. The area around the sensor did not display any visible evidence of significant changes that would lead to this behavior, making speculation on the cause difficult. One possible cause of this behavior is a gradual work-hardening of the stainless steel stud near this sensor. Due to the stud's relatively small cross-sectional area relative to previous specimen, localized strain could possibly have

caused strain hardening over time, eliciting a stiffer response and less slip. Another possibility is gradual slip of the LVDT itself in its mounting, leading to erroneous readings.

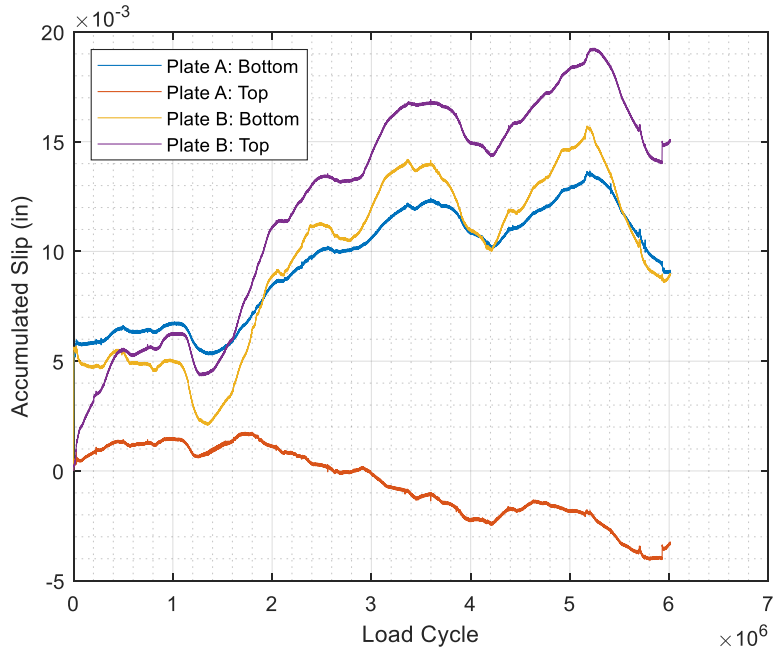

Figure 14: Specimen 4 - Apparent Slip Accumulated over Fatigue Testing

Figure 15 presents Specimen 4's average load-slip behavior over the course of fatiguing. In contrast to Specimen 3, which saw a quite large increase in average slip response, Specimen 4 did not see a very large increase, aligning more with Specimens 1 and 2. This provides further evidence that the large slips measured at the beginning of testing Specimen 3 may be due in part to concrete immaturity. The change in load-slip behavior over testing, as presented in Figure 15 is somewhat misleading, as the decrease in recorded slip at the top of Plate A pulls down the average slip at 6 million load-cycles. However, it is still evident that little hysteretic change can be observed, and that the loss of stiffness over testing (as indicated by the rotation of the load-slip curve) was small.

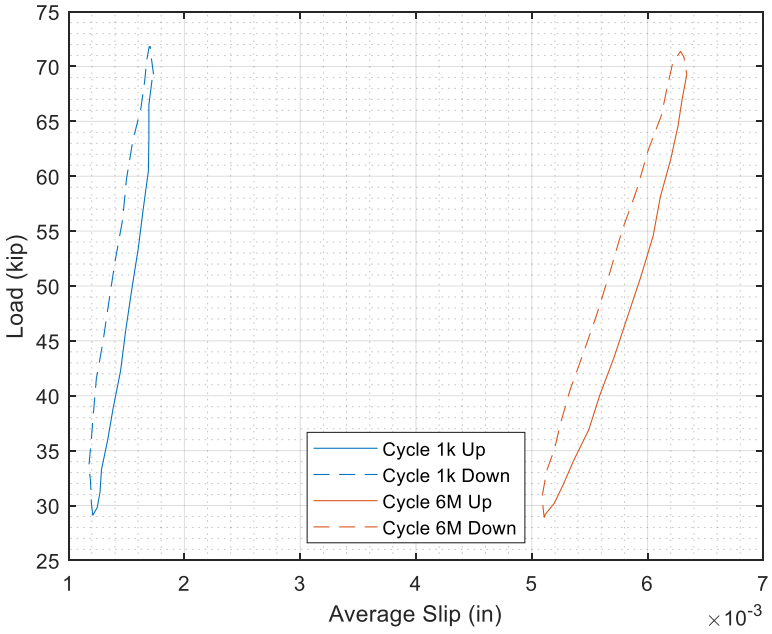

Figure 15: Specimen 4 – Average Load-Slip Behavior at Beginning and End of Fatigue Testing

2.4 Strength Tests

After Specimens 1 through 4 had been tested in fatigue, each specimen (including Specimen 5) was tested under strength-level conditions. Specimens were subjected to two levels of loading: service-level static loading applied to assess overall connection stiffness, and loads increasing to failure to characterize their ultimate strengths and failure modes. Table 2 summarizes the resulting connection stiffness, failure load, and shear flow across the connection at failure, as well as the AASHTO [4] Strength I shear flow for a representative 53-foot span bridge that could potentially use the connection designs tested in this study, and the HGMB [1, 3].

Table 2: Summary of Results of Strength Testing

Specimen	Stiffness (kip/in)	Failure Load (kip)	Shear Flow at Failure (kip/in)
1	460	160/173	3.64/3.93
2	445	172	3.91
3	399	151/181	3.43/4.11
4	405	152	3.45
5	386	96.6	2.20
AASHTO Strength I – Proposed Double CT Girder Bridge	-	-	2.49
AASHTO Strength I – Hampden Grist Mill Bridge	-	-	2.26

2.4.1 Protocol and Instrumentation

The five shear push-out specimens were tested under high service load to characterize their stiffness and unbounded ultimate loading to characterize strength. Load was applied using an Instron 300 kip servo-hydraulic actuator with integrated load and position measurement. During the stiffness-testing portion, load control was used with a compressive load rate of 330 lbf/s. LVDTs were mounted to the specimens (much like they had been during fatigue testing) to measure relative slip between the FRP plates and concrete blocks. During failure testing, position control was used with a compressive displacement rate of 0.05 in/minute, and the LVDTs were removed to prevent damage. All data were recorded at a sampling rate of 10 Hz.

The stiffness phase of strength testing was conducted in three monotonic load cycles. In each cycle, compressive load was applied up to the mid-point load from fatigue testing (49 kip) and was then removed to near zero. Once stiffness load-cycling had been completed, the LVDTs were removed and the specimens loaded to failure, with failure being defined as a large decrease in measured load, after which a specimen was unable to recover lost load or carry additional load. Before strength testing, concrete cylinder samples were compression tested to failure for applicable specimens (1, 2, and 5) to evaluate concrete strength [5]. The results of cylinder testing are presented in Table 3. Results for specimens 3 and 4 are noted not applicable as no cylinders were provided for strength testing. However, it can be reasonably assumed that the measured compressive strength would be somewhat larger than the 28-day strength reported by S.W. Cole due to the elapsed time between the reported cylinder tests and specimen strength level testing.

Table 3: Push-Out Specimen Concrete Compressive Strength before Strength Testing

Specimen	Date of Cylinder Tests	f'_c (psi)	Shear Connector
1, 2	3/4/2021	12,100	Straight GBolt
3, 4	N/A	N/A	1”, ¾” Stainless Rod
5 (Not Fatigued)	3/29/2021	8,220	Hooked GBolt

2.4.2 Results

2.4.2.1 Specimens 1 & 2

Figures 16 and 17 present the results of stiffness testing performed on Specimens 1 and 2 respectively. From these plots, two observations can be made. First, the loading phase of stiffness ramping was generally linear, whereas the unloading branches were somewhat nonlinear and did not follow the loading branch closely. Secondly, the second and third loading ramp paths were quite similar to one another, but differed from the first. The difference between the first and subsequent loading ramps is slight, but more pronounced for Specimen 2. The reason for these differences and the nonlinearity of the unloading branch is not immediately apparent, although

speculation can be made. For instance, this may have been caused by a small amount of damage incurred during the first load ramp or from time-dependent deformation recovery of the neoprene pad placed beneath specimens during testing. In either case, the average stiffnesses of Specimens 1 and 2 were 460,000 lbf/in and 445,000 lbf/in respectively.

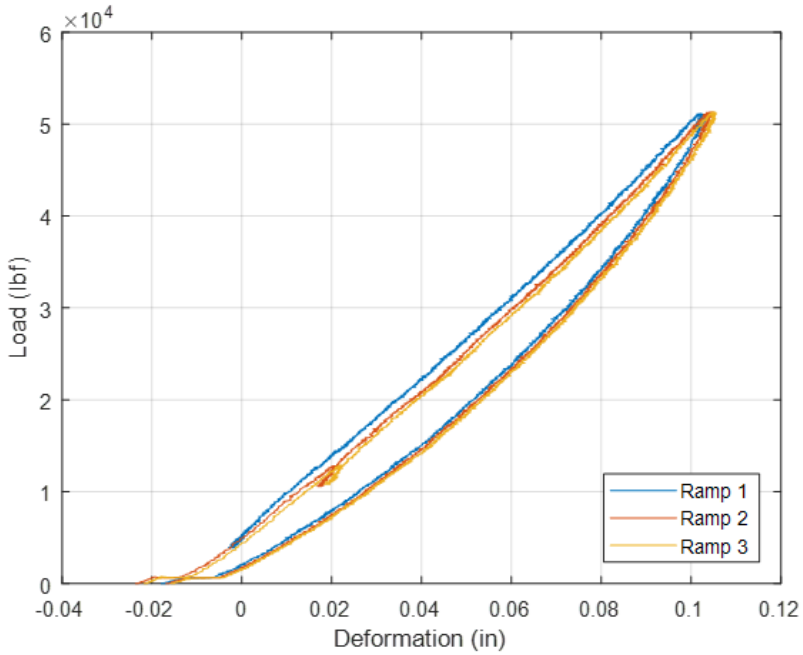

Figure 16: Specimen 1 – Service-Load Stiffness Testing

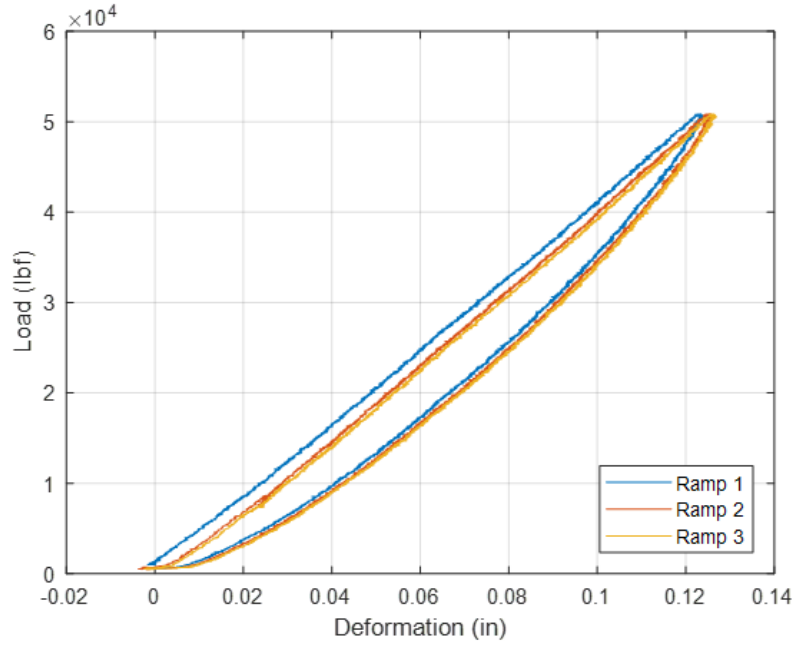

Figure 17: Specimen 2 – Service-Load Stiffness Testing

Some additional information can be gleaned from the slip measured between FRP plates and concrete over the course of stiffness testing. These were averaged across the four LVDT's attached to each specimen and are plotted in Figure 18 for both specimens. As can be seen, the maximum and minimum recorded slips were roughly constant, accounting for a slight zero-drift in the LVDT readings. Additionally, the slips recorded during unloading were reasonably similar to those recorded during loading. This would seem to indicate linear slip behavior, suggesting that the slight nonlinearity observed from the load-displacement plots is not due to the specimens themselves, and rather comes from external sources such as time-dependent neoprene decompression.

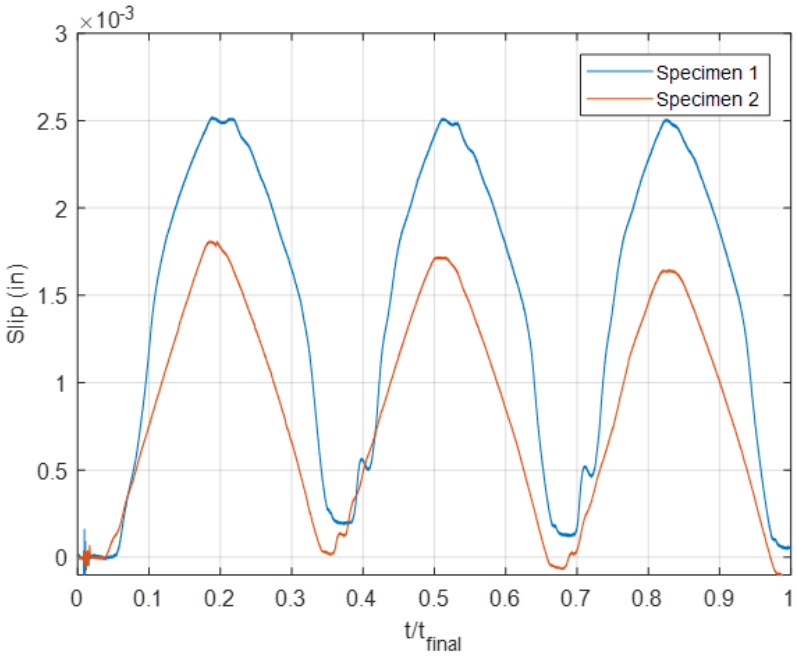

Figure 18: Specimens 1 & 2 – Average Slip Data

Figures 19 and 20 present the load-deformation curves recorded during failure testing of Specimens 1 and 2, respectively. As with specimens tested to failure as part of previous studies [1-3], the ultimate behavior of these specimens was characterized by an initial, roughly linear load-deformation response up to failure. For both these specimens, initial failure was due to crushing of the concrete block with significant cracking and spalling, usually around top or bottom corners. As seen in Figure 20, the failure of Specimen 2 at around 172,300 lbf led to an immediate drop in load, after which little additional load was carried. However, the initial failure of Specimen 1 at around 159,400 lbf led to an immediate drop in load which was recovered and surpassed, with secondary failure occurring under a load of around 172,700 lbf, which is close to the failure load of Specimen 2. It is possible that at the initial failure, some of the FRP and/or concrete ridged in the connection experienced shear failure (due to concrete porosity, lack of fiber penetration, etc.). After this, the remaining intact connection components were able to carry the additional load until concrete crushing had occurred. This crushing failure can be seen in Figures 21 and 22 for

Specimens 1 and 2, respectively. It can be assumed that during crushing failure, shear failure of the concrete ridges also occurred, as can be seen in Figures 21 and 22.

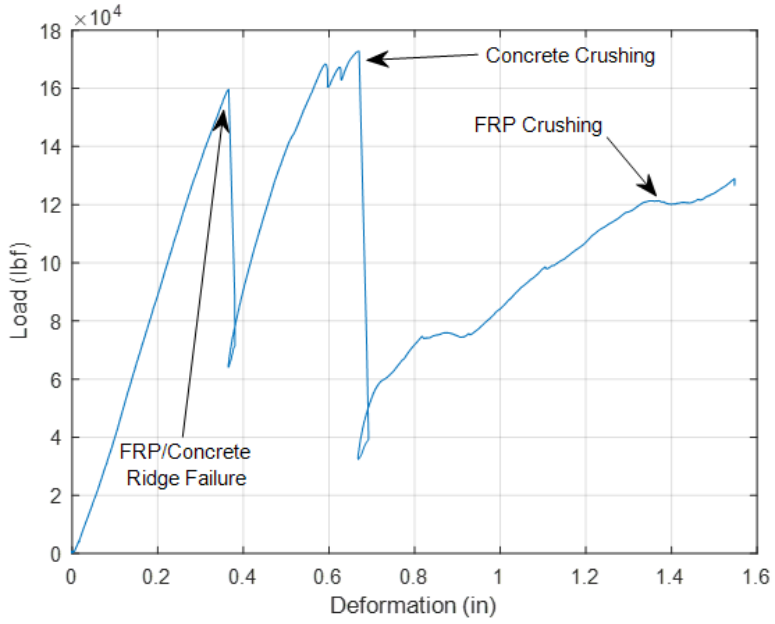

Figure 19: Specimen 1 – Ultimate-Load Strength Testing

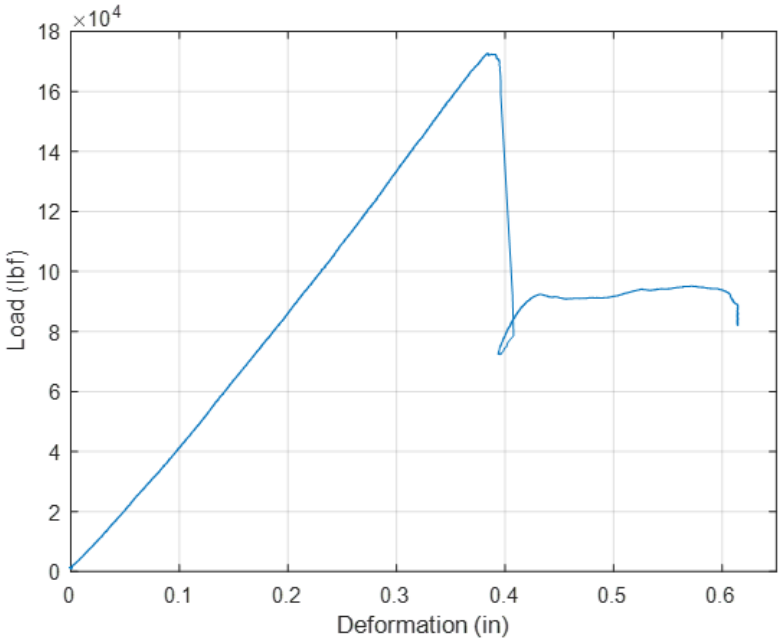

Figure 20: Specimen 2 – Ultimate-Load Strength Testing

Figure 21: Specimen 1 – Concrete Crushing Failure

Figure 22: Specimen 2 – Concrete Crushing Failures

2.4.2.2 Specimens 3 & 4

Figures 23 and 24 present the results of stiffness testing of Specimens 3 and 4, respectively. Similar to Specimens 1 and 2, the load-deformation response of Specimens 3 and 4 during stiffness testing was characterized by roughly linear response during loading and nonlinear response during unloading. Additionally, the responses during load ramps 2 and 3 were again similar to one another, with the response during the first ramp being slightly shifted. These similarities to the behavior from Specimens 1 and 2 suggests that the linearity of Specimens 3 and 4 is also affected by a factor outside of the specimen itself. The average calculated stiffnesses were 399,000 lbf/in. and 405,000 lbf/in. for Specimens 3 and 4, respectively. These are somewhat more compliant than Specimens 1 and 2, which is reasonable considering their lower concrete compressive strengths (correlating to lower concrete elastic moduli [4]).

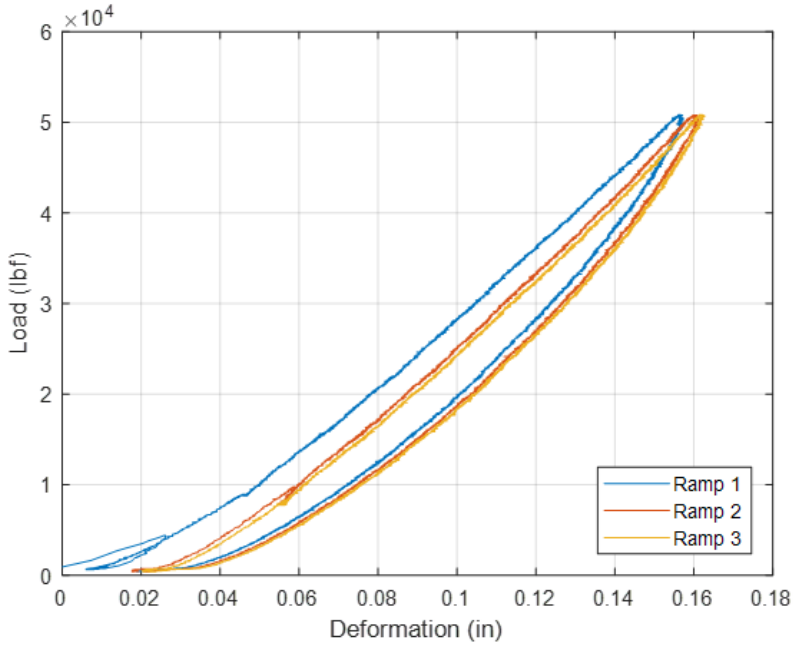

Figure 23: Specimen 3 – Service-Load Stiffness Testing

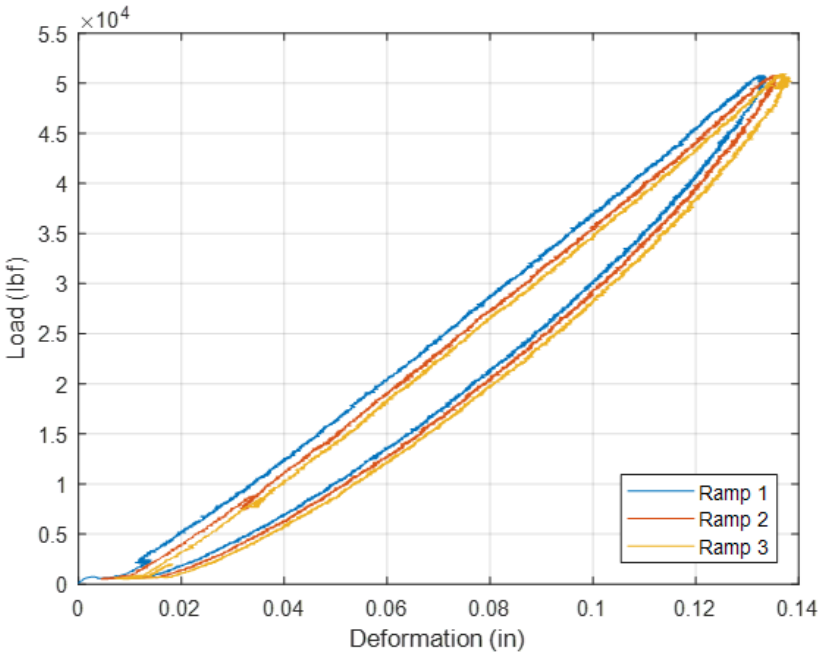

Figure 24: Specimen 4 – Service-Load Stiffness Testing

Figure 25 presents the average slips recorded during stiffness testing of Specimens 3 and 4. As can be seen, these specimens behaved similarly to Specimens 1 and 2, with the magnitudes of maximum and minimum slips recorded staying roughly stable across subsequent load ramps, and similar loading and unloading behavior. However, Specimen 3 experienced much greater average slips than did any of the other specimens. This is consistent with the results of fatigue testing, wherein Specimen 3 exhibited the largest final slips of any fatigued specimen. The reasons for this are not immediately apparent, as this specimen did not have any outwardly visible differences from other specimens and had a nearly identical stiffness to Specimen 4.

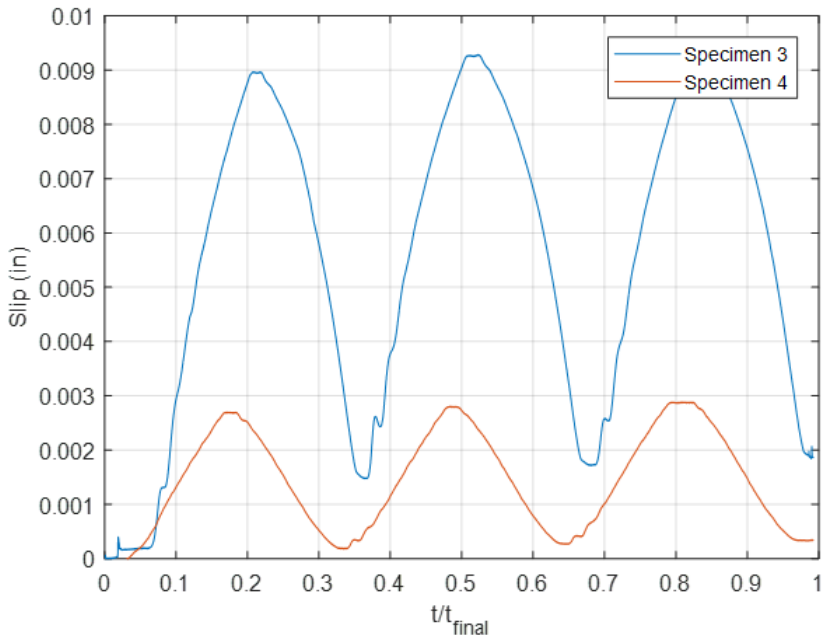

Figure 25: Specimens 3 & 4 – Average Slip Data

Figure 26 presents the load-deformation response of Specimen 3 during failure testing. As with the previous specimens, this Specimen's behavior was initially characterized by a roughly linear regime. However, after this initial, linear regime, it exhibited behavior that differed from the previous two. Specimen 3 experienced a significant loss in load carried at a load of around 150,600 lbf. After this drop, it was able to sustain additional load surpassing its initial failure point until experiencing a full loss of marginal load capacity at around 180,900 lbf. This secondary load-path is less stiff, and is characterized by significant nonlinearity.

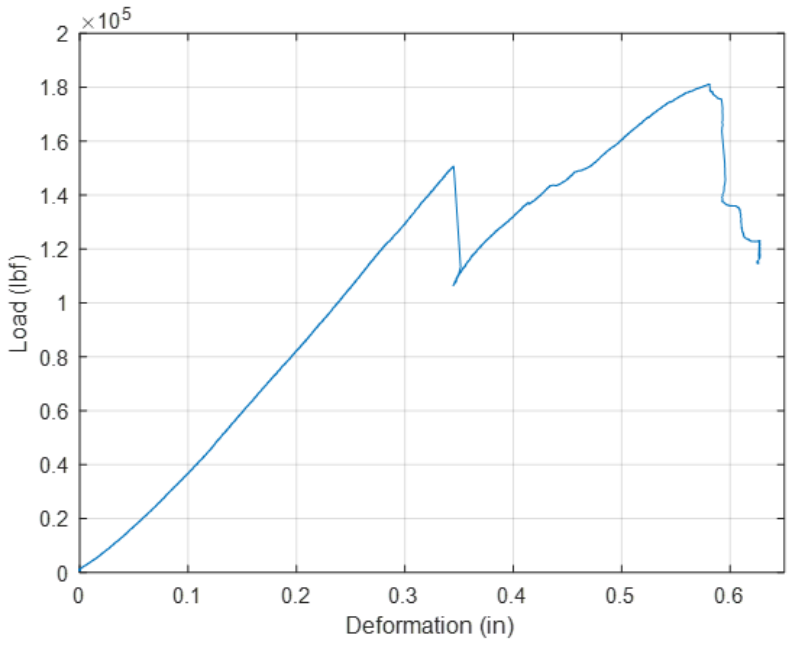

Figure 26: Specimen 3 – Ultimate-Load Strength Testing

Examination of Specimen 3 did not reveal the concrete compressive failure characteristic of the first two specimens, with only a small portion of the bottom of the block spalling from the main block, as seen in Figure 27. However, as seen in Figure 28, one of the FRP plates under the actuator's load-head experienced significant crushing and delamination. During removal of the FRP plates from the concrete block, it was observed that the stainless steel studs were in direct bearing with the plates, making removal difficult, and that nearly all of the ridges cast into the concrete block had experienced shear failure. From these observations, the specimen's progression of failure can be hypothesized. At the initial failure point (150,600 lbf), the connection's concrete ridges began to fail in shear, causing the stainless studs to be loaded by direct bearing. These then began to yield (accompanied by the shear failure of additional ridges), as evidenced by the nonlinearity of the secondary load-path. It is unclear whether the final drop in load was due to concrete compressive failure (Figure 27) or FRP crushing (Figure 28). However, as they occurred on opposite sides of the Specimen, it is possible that one led to the other as a loss of stiffness on one side of the Specimen led to additional load being taken by the other, which exceeded its corresponding capacity.

Figure 27: Specimen 3 – Minor Concrete Spalling

Figure 28: Specimen 3 – FRP Crushing

Figure 29 presents the load and deformation data recorded from Specimen 4 during failure testing. Behavior was roughly linear up to a load of around 123,700 lbf, after which the specimen experienced some mild softening. Peak load occurred at around 150,800 lbf, which was followed by a moderate loss of load and inability to recover or carry additional load. Investigation of the failed specimen revealed that the initial softening was likely due to concrete ridge shear failure, as can be seen in Figure 30. The drop in load after peak is likely due to a concrete crushing failure

(visible from a large spall at the specimen's bottom in Figure 30) which was followed by stud yielding and pullout, visible in Figure 31.

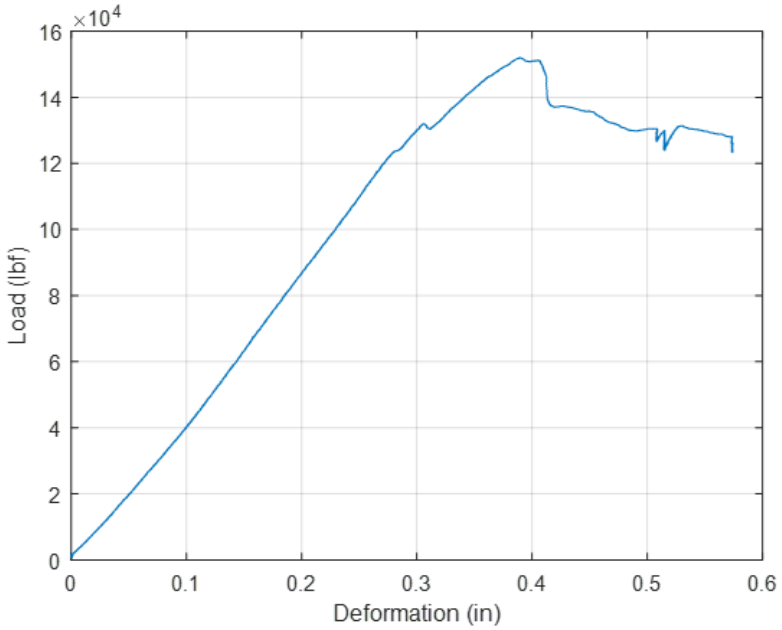

Figure 29: Specimen 4 – Ultimate-Load Strength Testing

Figure 30: Specimen 4 – Concrete Ridge Shear Failure and Spalling

Figure 31: Specimen 4 – Stainless Stud Yielding and Pullout

2.4.2.3 Specimen 5

As mentioned previously, Specimen 5 was manufactured with FRP ridges shaved to half their original height before concrete was cast to simulate poor quality ridge infusion. This smaller-than-designed ridge amplitude was therefore mirrored by the concrete when it was poured, leading to a significant reduction in strength relative to the previous specimens. This disqualifies the specimen from being used as a control for quantitative comparison with previous specimens. However, because it was not subject to fatigue loading and did not suffer damage during stiffness testing, qualitative trends in the specimen's stiffness behavior can be compared with previous specimens.

Figure 32 presents the results of stiffness testing performed on Specimen 5. This specimen's load-deformation behavior was qualitatively similar to that of the previous specimens. Its response during loading cycles was roughly linear, while its response during unloading was nonlinear and displayed some hysteretic deformation. In addition, the response during the second and third load ramps were stiffer and slightly offset from the first. As noted in Table 2, on average Specimen 5's stiffness (386,000 lbf/in.) was around 85% that of Specimens 1 and 2. However, this difference in stiffness is reasonable considering Specimen 5's lower compressive strength. As shown in Table 3, on the day of testing, concrete cylinders cast concurrently with Specimens 1 and 2 exhibited an average compressive strength of 12,100 psi, compared with Specimen 5's 8,220 psi. Using AASHTO's [4] formula for concrete elastic modulus (a function of compressive strength), the ratio of Specimen 5's concrete elastic modulus to that of Specimens 1 and 2 is around 82.4%, close to the measured 85% for the specimens as a whole. This suggests that, for service-level loading, the connection's stiffness is not highly dependent on ridge quality, but rather depends more highly on concrete stiffness.

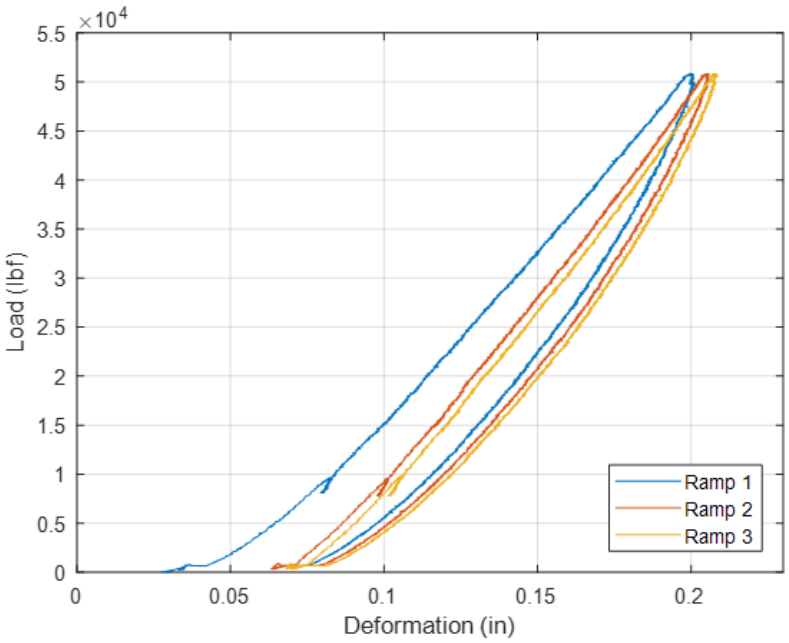

Figure 32: Specimen 4 – Service-Load Stiffness Testing

Additional differences between the stiffness test behavior of Specimen 5 and the previous, fatigue tested specimens can be seen in Figure 33, which presents the average slips between concrete and FRP plates recorded during stiffness testing. In contrast to previous specimens, a significant amount of irrecoverable slip was incurred during each load ramp. This can be seen as the slip not returning to near-zero after load is removed. This behavior is consistent across both FRP plates at both the top and bottom, as seen in Figure 34. Both Figures 33 and 34 also display significant asymmetry between the slips recorded during loading and unloading, as well as a decreased signal-to-noise ratio in recorded slip as compared with previous specimens. This behavior is possibly due to the specimen being in its "virgin" state, not having been significantly loaded under previous fatigue testing. It is plausible that this irrecoverable slip, load-unload asymmetry, and noisy signal were also characteristic of the other specimens during their first fatigue cycles as imperfections in connections and tolerance gaps were taken up in a "wear-in" period. This is further evidenced by the large amount of slip each previous specimen accumulated early in fatigue testing (see Figures 6, 8, 12, and 14).

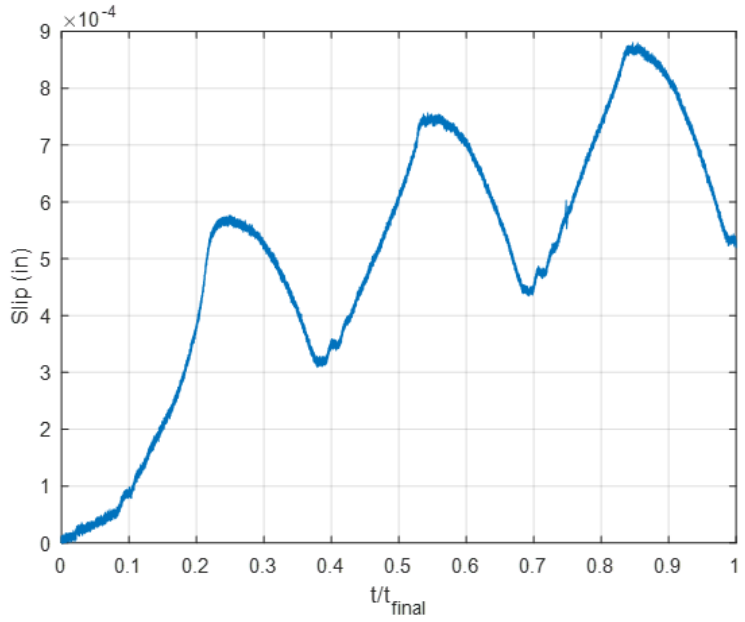

Figure 33: Specimen 5 – Average Slip Data

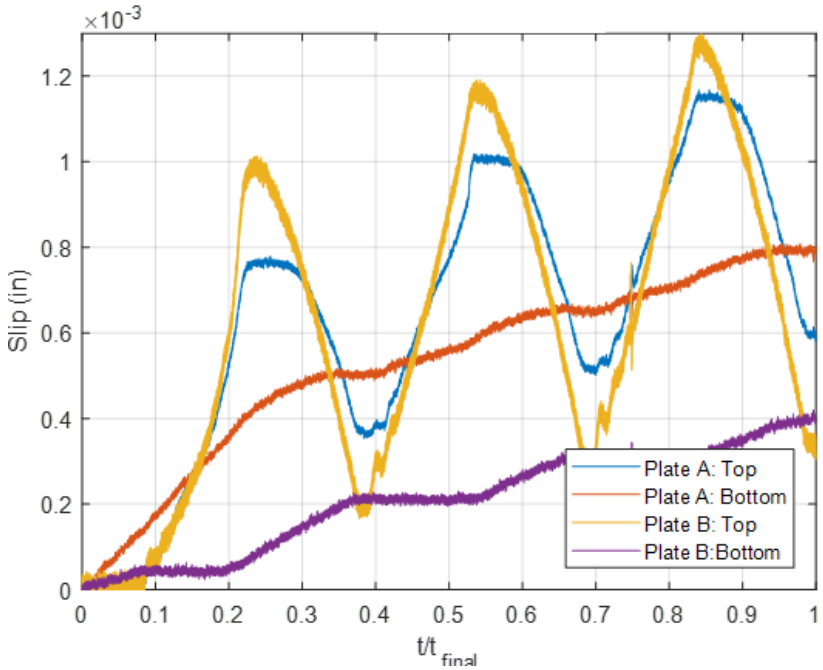

Figure 34: Specimen 5– All Slip Data

Figure 35 presents Specimen 5's load-deformation response during failure testing. As can be seen, the specimen's response is qualitatively very similar to previous specimens (especially Specimens 1 and 2), with an initial, linear range up to a well-defined failure point. After this point a significant amount of load was dropped with some recovered during a nonlinear, softening phase

and a final point at which no additional load can be carried. Quantitatively, Specimen 5 failed at a load of 96,600 lbf, a 40% reduction from Specimen 1 and a 44% reduction from Specimen 2. This reduction in failure load is reasonable considering the loss of ridge interlock resulting from shaving the height of the initial FRP ridges, as well as the specimen's lower concrete strength.

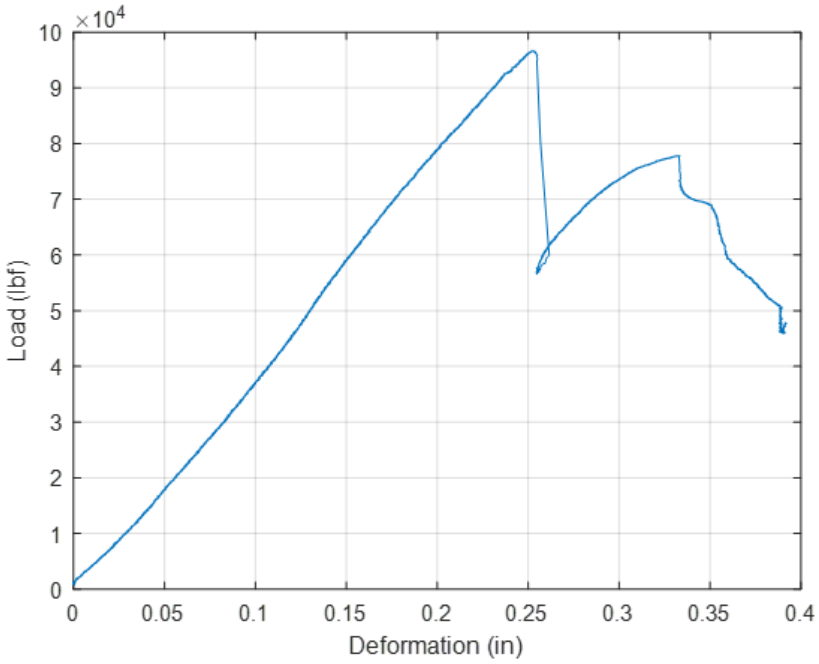

Figure 35: Specimen 5 – Ultimate-Load Strength Testing

Inspection of Specimen 5's FRP-concrete interface after testing provides some additional insight into the possible series of events leading to complete failure. The damage sustained by the two interfaces, by both the concrete and FRP, was quite different. Side A (shown in Figure 36) sustained heavy damage, with all of the positive concrete ridges (and in fact some of the negative ridges as well) experiencing shear failure, and significant bearing damage occurring at the stud-holes in the FRP. Contrary to this, Side B (shown in Figure 37) experienced much less concrete damage and no visible FRP bearing damage. It can be hypothesized that most of the concrete damage from Side A occurred around the peak loading, which led to the immediate drop in load seen in Figure 35. After this, much of the additional load was shed to Side B, with the majority of load carried by Side A resulting from the FRP bearing directly on the studs. From there, the concrete ridges on Side B began to fail progressively, leading to the softening seen in Figure 35 after peak load.

Figure 36: Specimen 5 – Side A Heavy Damage (Left: Concrete, Right: FRP)

Figure 37: Specimen 5 – Side B Moderate Damage (Left: Concrete, Right: FRP)

2.5 Conclusions and Future Work

The results of fatigue and strength testing of push-out specimens using the ridged concrete-FRP shear connection system continue to indicate its ability to act as a viable shear connection system between FRP bridge girders and composite concrete decks. These tests also indicate that the system remains viable when corrosion-resistant studs are used to provide perpendicular clamping force in place of conventional steel studs. Each of the specimens tested in fatigue was able to withstand the target 6 million cycles of AASHTO [4] Fatigue I shear loading without failing or incurring significant permanent damage. Additionally, each of these previously fatigued specimens' shear flow resistance at failure exceeded the AASHTO Strength I shear flow for a representative 53-foot span bridge design by a minimum of 38%, and for the HGMB by a minimum of 53% as reported in Table 2. However, the final, non-fatigued specimen using intentionally poor-quality FRP ridges was not able to provide the required shear flow resistance for either the representative 53-foot span bridge or the HGMB.

Both fatigue and strength testing of the push-out specimens indicate that the behavior of the connection is highly dependent on the strength and quality of the concrete, especially the concrete making up the cast-in shear ridges. Specimens 1 and 2 were cast by ACInd. under production quality standards and began fatigue testing well after the 28 days from casting assumed to develop full compressive strength. These both behaved similarly (discounting the effects of the cracked FRP nut from Specimen 2) with very small accumulated slips which stayed relatively constant after an initial "wearing-in" period. In contrast, the specimens cast concurrently with the HGMB (Specimens 3 and 4) were of lower overall concrete quality, as they used a lower strength concrete mix and quality procedures available in the field. Additionally, Specimen 3 began fatigue testing at an age of only 10 days, less than half the time required to reach full maturity and compressive strength as specified by AASHTO [4]. These factors seem to have affected these Specimens' fatigue behavior, allowing for much larger initial slips and greater variability than what was exhibited by the first two specimens. In the case of Specimen 3, the fatigue tests results are likely a conservatively lower bound on actual fatigue performance, since in a real structure fatigue occurs over a much longer time frame and only after the deck has fully cured.

In addition to the evidence provided by the results of fatigue testing, results from strength testing provide further evidence that the behavior of the connection is highly dependent on the quality and strength of the concrete making up the ridges. The first specimens cast by ACInd. (Specimens 1 and 2) failed suddenly and at a high load (around 170,000 lbf) due to concrete crushing, with the ridged connection relatively unaffected. In contrast, the in-situ cast specimens (3 and 4) began failure due to shearing of the connection's concrete ridges, leading to softening and a progressive failure at lower loads (around 150,000 lbf). Although progressive, ductile failure is often desirable over sudden brittle failure in design, the difference in maximum load and failure type between the two specimen classes shows the connection's high dependence on concrete quality and strength.

Comparison against the results of strength testing of Specimen 5 indicate that the quality of the FRP ridges also plays a significant role in overall connection strength. The connection's stiffness was comparable to that of the original ACInd.-cast specimens, considering its smaller concrete compressive strength. However, the disparity in connection strengths between these specimens is too great to fully attribute to differences in concrete strength, and it is probable that this additional disparity is due, at least in part, to the reduced FRP ridge quality.

Comparison of results from this investigation with those from the most closely-related previous study [1, 3] suggest that application of pretensioning torque to the connection's clamping studs has little effect on connection stiffness, but can affect its strength. Stiffness testing of pretensioned stainless steel stud specimens reported in reference [1, 3] yielded an average connection stiffness of around 412,000 lbf/in, whereas the non-pretensioned stainless stud specimens of the current study yielded an average stiffness of about 402,000 lbf/in, a difference of less than 3%. However, the differences in average failure loads were more significant between the studies, around 171,000 lbf and 152,000 lbf respectively, a difference of 11.1%. Although other independent variables exist between these specimens, which undoubtedly contributed to this difference, enough similarities exist to confidently conclude that pretensioning contributes to connection strength. In addition, the results of the previous study [1, 3] showed pretensioned, grade 5 bolted connections to have an average failure load of around 206,000 lbf, whereas the present study showed non-pretensioned GBolt connections to have an average failure load of 166,000 lbf, and non-pretensioned 18-8 stainless rod connections to fail at an average load of 152,000 lbf. Both these failure loads represent a significant reduction in strength as compared with the grade 5 specimens of the previous study, but still represented shear flows at failure significantly in excess of those calculated for the representative 53-foot span bridge and HGMB. This suggests that non-pretensioned connections could be a viable alternative for similar structures, which could eliminate the possibility of corrosion-induced damage and associated maintenance.

Results from this study demonstrate the ridged FRP-concrete shear connection's viability and ability to withstand the horizontal shear flow expected at ultimate levels for double CT girder bridges with a variety of design parameters. However, the number of independent variables that were changed between specimens within the study and as compared with previous studies limits the conclusions that can be drawn regarding their effects on fatigue degradation, stiffness, and strength. Casting the concrete making up specimens in three separate batches and using two separate concrete batch sources caused large differences between specimen behaviors, and limited the observable differences between types of clamping stud, which was of greater importance to the study's goals. Further, changing Specimen 5 from a control specimen to a specimen with an additional independent variable changed eliminated the opportunity to detect fatigue-related degradation in stiffness and strength. In addition, because only a single specimen was tested that had its FRP ridges shaved to simulate poor infusion quality, no conclusions regarding the effects of FRP ridge quality can be confidently made beyond the general observation that this specimen did not exhibit adequate strength for the target applications.

Future studies should consider only a single concrete source and mixture, with all specimens allowed adequate curing time before testing. This will eliminate concrete strength and quality as independent variables, making changes in behavior among specimens more easily attributable to clamping method. Additionally, the effect of pretensioning should be better quantified for a specific connector that is anticipated to be widely used in the future. Realistically achievable, sustained levels of pretension should be determined and applied, as it is possible that modest amounts of pretension could have a positive effect on performance. Finally, if ridge size and quality are a concern, the effect of these parameters needs to be assessed with a carefully designed test matrix.

3 Full-Scale Double CT-Girder Creep Deflection

3.1 Introduction

It is well known that FRP and concrete exhibit visco-elastic behavior over time leading to the phenomenon we know as creep, an increase in deflection over time under a constant state of stress [6-8]. Additionally, other composite FRP-concrete sections used as the main structural members of bridges are subject to creep deflection and rupture, with these limit states addressed in design [9]. It can therefore be safely assumed that the double CT girder would likely display creep behavior and that this behavior must be both understood and accounted for in design. As a first step in gaining this understanding, UMaine tested one half of a double CT girder section (a full double CT girder cut length-wise and consisting of one FRP girder, and both the lower, precast, and upper, cast-in-place deck sections within the girder's tributary width) under its own weight in creep. An image of the creep girder specimen, hereafter referred to as "UTC-1", can be seen in Figure 38. This test simulates a CT girder, which, after having been manufactured, was fully supported until its upper deck section had fully cured, after which supports were removed and no further dead loads or sources of stiffness introduced.

Figure 38: UTC-1 Creep Girder Specimen

3.2 Specimen Manufacture and Testing Procedure

The creep girder specimen, referred to hereafter as "UTC-1" was manufactured collaboratively by AIT Bridges and ACInd, and can be seen in Figure 38. AIT Bridges manufactured the hybrid girder using the vacuum infusion process and a reinforcement layup similar to that of a bridge that will be constructed in Hampden, Maine. ACInd. cast the specimen's deck at its plant in Auburn, Maine on December 18, 2020, and was subsequently delivered to the Center. During manufacturing and shipping, care was taken to support the girder fully so as to minimize the load carried directly by the specimen in bending. This ensured that, once set on bearing blocks, the specimen would be in near-virgin state and without having experienced significant creep deformation.

Upon delivery to the Center on February 17, 2021, UTC-1 was immediately placed on concrete bearing blocks and instrumented with dial indicators. Three indicators were used, one at either end which measured deflection relative to the concrete bearing blocks, and one at midspan which measured deflection relative to the floor. The indicators at the girder's end and at midspan had ranges of 1 in. and 4 in. respectively, and each had a resolution of ±0.0005 in. These are shown in Figure 39. Immediately upon removal of support, deflection measurements commenced. Initially, measurement frequency was once every 10 minutes until the lab closed in the evening. Beginning the next morning (February 18, 2021), frequency was set to one measurement every 30 minutes for several hours. After the rate of creep had slowed sufficiently, the frequency was

reduced to 4 measurements per day for an additional 2 days, 3 measurement per day for an additional 4 days, and finally 2 measurements per day thereafter. Measurements were taken on weekdays only and only during lab business hours. The final measurement was taken on September 20, 2021, giving a total measurement period of 215 days. In addition to deflections, each measurement also included ambient lab temperature and humidity with a portable thermometer/humidity sensor, and surface temperature of the girder and concrete around the areas of the dial indicators using an infrared thermometer.

Figure 39: Deflection Measuring Dial Indicators

Between February 22 and 23, 2021, it was noticed that the displacement measured at midspan was decreasing significantly with time, contrary to the expected growth in creep displacement. It was determined that the midspan dial gage had begun to slip in its mounting, leading to the erroneous readings. For this reason it was reset and remounted using a more rigid setup. To account for the disruption, the distance from the floor to the top of the deck was measured at midspan and at the two ends of the specimen using a tape measure. The average difference between end and midspan heights was taken as the new reference creep deflection. Accounting for the tape measure's 1/16" precision, this initial creep was taken as 0.180 in.

For the purposes of comparison with measured creep deflection, the girder's instantaneous mid-span self-weight deflection was determined. A more accurate and representative comparison would come from measurement of the instantaneous elastic deflection itself. However, due the sequence of events and method by which UTC-1 was supported and the need for expedience in taking initial creep measurements, this was not possible. Instead, the deflection was calculated based on the specimen's nominal material and geometric properties using classical lamination

theory. This deflection equaled approximately 1.18 in., a ratio of deflection to span length of about 1/568.

As an additional point of comparison, the specimen's approximate shrinkage deflection was computed for elapsed times of one day to one year after casting. These can be seen plotted in Figure 40 with key dates in testing noted. To estimate these deflections, uniform shrinkage strain in the concrete at each time-step was estimated per AASHTO [4] in Equation 1, where ε_{sh} is the estimated uniform shrinkage strain in the deck at a particular time after casting and k_s, k_{hs}, k_f, and k_{td} are empirical factors accounting for the deck's shape, the ambient humidity, the concrete's initial strength, and the elapsed time, respectively. To ensure plane sections, the shrinkage strain and a nonuniform strain distribution causing internal stresses (ε_σ) were summed and equated to the sum of an axial (ε_a) and bending (ε_ϕ) strain in Equation 2. By enforcing moment equilibrium, the curvature was found through Equation 3, in which A_c is the cross-sectional area of the concrete, $\bar{y}$ is the composite centroidal height, y_c is the height of the concrete centroid, and I_T is the transformed moment of inertia for the composite section. Separately, the curvature was taken as the second derivative of the deflection caused by shrinkage and integrated twice to obtain an expression for the deflection as seen in Equations 4 and 5 in which v is shrinkage displacement of the girder at a position x along its span length L. By substituting Equation 3 into Equation 5 and setting the position at midspan ($x = {}^{L}/_{2}$), a straightforward estimation of midspan deflection from shrinkage could be obtained.

$$\varepsilon_{sh} = k_s k_{hs} k_f k_{td} * 0.48 \times 10^{-3} \qquad \text{Equation 1}$$

$$\varepsilon_{sh} + \varepsilon_\sigma = \varepsilon_a + \varepsilon_\phi \qquad \text{Equation 2}$$

$$\phi = \frac{1}{I}\int \varepsilon_{sh} dA = \frac{\varepsilon_{sh} A_c (\bar{y} - y_c)}{I_T} \qquad \text{Equation 3}$$

$$\frac{d^2 v}{dx^2} = \phi \qquad \text{Equation 4}$$

$$v = \frac{\phi x}{2}(x - L) \qquad \text{Equation 5}$$

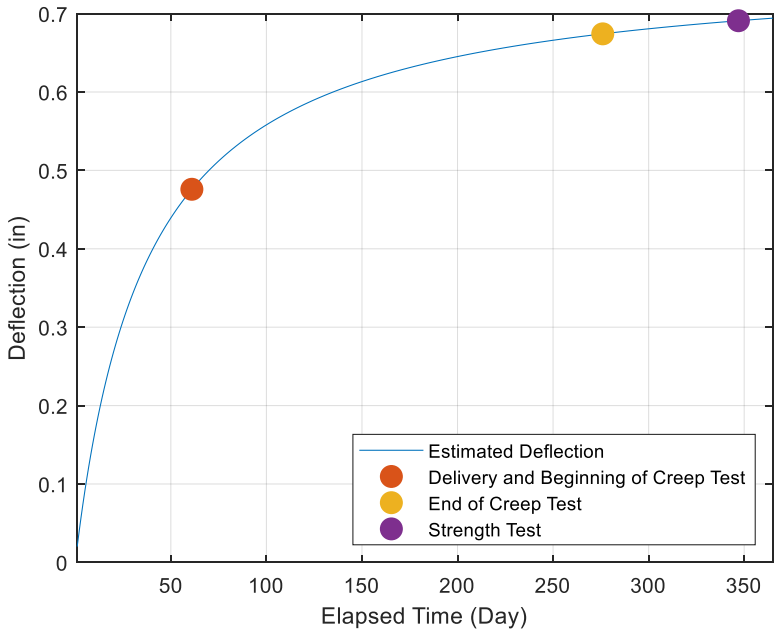

Figure 40: Estimated Shrinkage Deflection

3.3 Results and Discussion

The midspan creep deflection over the course of testing was calculated as the average difference between measured displacement at girder ends and midspan, plus the initial offset value after the February 23 reset. This is plotted in Figure 41 as a function of elapsed time. As can be seen, from the beginning of recording to around 1,500 elapsed hours (on April 26, 2021, around 63 days from test reset) creep tended to increase rapidly with time, although the rate of creep tended to decrease gradually. It is interesting to note as well that, during this period, large spikes in creep deflection are visible at regular intervals, after which creep deflections tend to normalize. These spikes correspond with measurements taken on Monday mornings after the OWL had cooled due to inactivity over the previous weekend. Cooling of the girder will result in shrinkage of the deck, although less shrinkage is expected for the FRP section because the unidirectional carbon fiber in bottom flange likely has a coefficient of thermal expansion of near zero. Therefore, thermal shrinkage of the concrete deck will result in upward curvature of the beam, producing additional deflections that will reverse as the deck warms following re-opening of the lab.

After the initial 1,500 elapsed hours, the rate of creep deflection decreased significantly, with average creep deflection remaining relatively constant. From around 2,250 hours (94 days from test reset, June 1, 2021) to the completion of testing, measured creep exhibited significant variability with large spikes and dips. However the average creep remained relatively constant until 4,500 hours, at which time deflection increased significantly. This immediate jump in creep deflection cannot be fully explained, but also corresponds with a decrease in average ambient temperature, as discussed later. In addition to deflection, the OWL's ambient relative humidity

and temperature were recorded to investigate their possible effects on creep. These are presented in Figures 42 and 43, respectively both as raw measurement data and clarified with a Gaussian moving average filter, window length of 4.

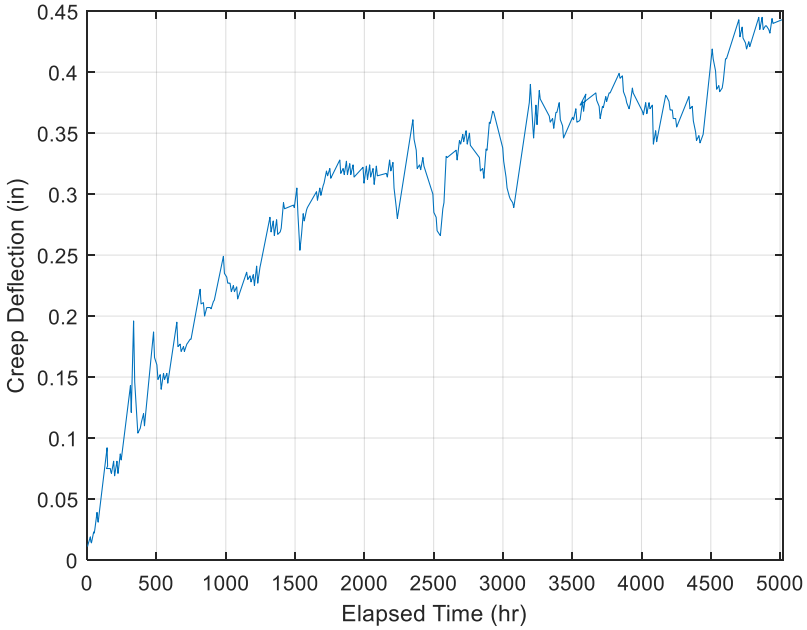

Figure 41: Recorded Creep Deflection

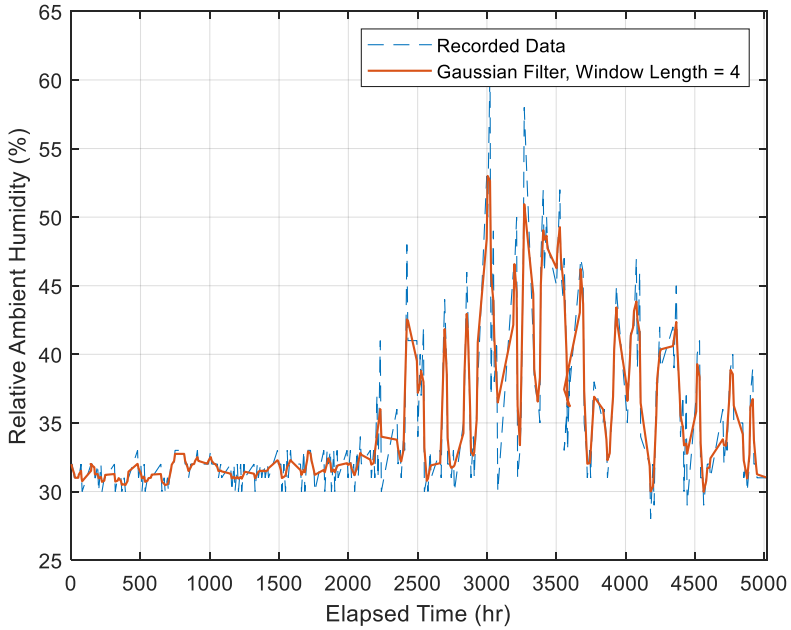

Figure 42: Recorded OWL Relative Humidity

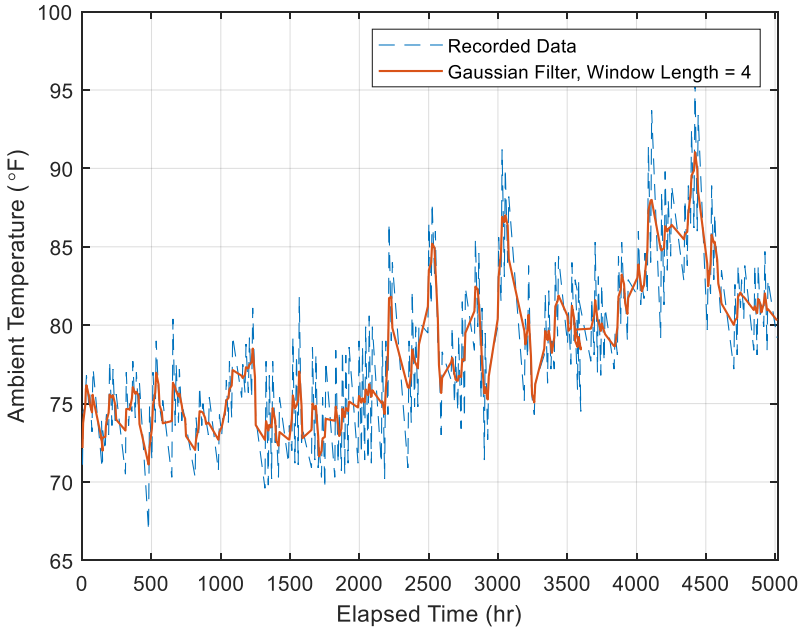

Figure 43: Recorded OWL Temperature

The apparent creep deflection presented in Figure 41 appears to vary logarithmically with time. To test this observation, a logarithmic function was fit to the data by nonlinear least-squares regression. This resulted in a best-fit curve described by the function

$$\delta(t) = 0.0063\sqrt{t} \qquad \text{Equation 6}$$

where δ is the predicted creep deflection in inches and t is the elapsed time in hours. The predicted and recorded deflection are compared in Figure 44, which shows that the model's predictions agree well. This is further confirmed by the coefficient of determination between measured and predicted creep deflection, equaling 0.964. In addition, using an approximate neutral axis height y, the creep strain can be estimated as

$$\varepsilon(t) = \frac{48y * \delta(t)}{5L^2} \qquad \text{Equation 7}$$

where L is the span length of the girder. These strains were used to create a Findley's power law [11] model to predict midspan creep strain at the girder's extreme tension fiber, again determining the required coefficients by nonlinear least-squares regression. This model is described by the function

$$\varepsilon(t) = 5.68 * 10^{-4} + 5.54 * 10^{-4} * t^{0.429} \qquad \text{Equation 8}$$

It should be noted that the strains predicted by Eq. 3 are in units of percent. The strains predicted by Equation 8 are presented in Figure 45, which shows excellent agreement. This is further confirmed by the coefficient of determination of the pair, which equals 0.969. The maximum creep

strain of 0.022% ≈ 220 με, or about 2.4% of the average strain at failure of the carbon bottom flange of 9180 με observed in the beam test reported by Davids et al. [13].

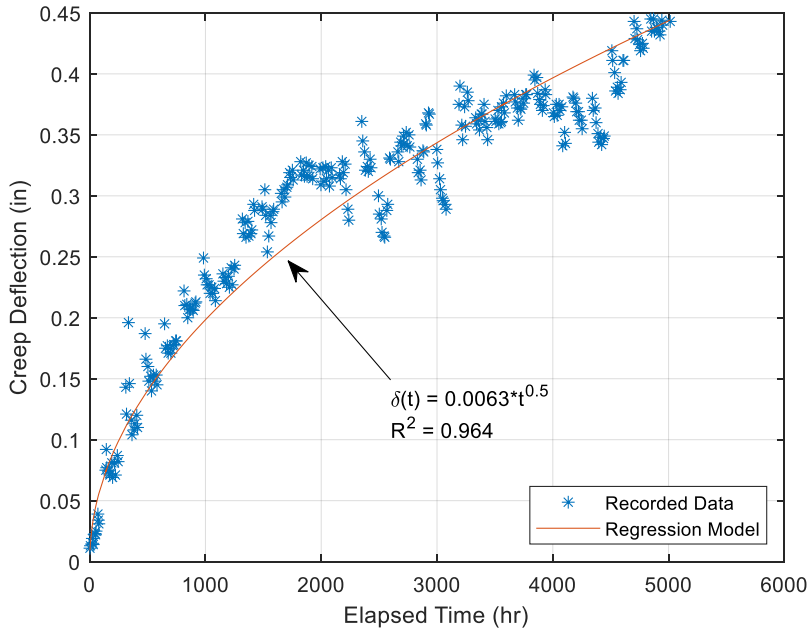

Figure 44: Comparison of Recorded Creep Deflection and Regression Model Prediction

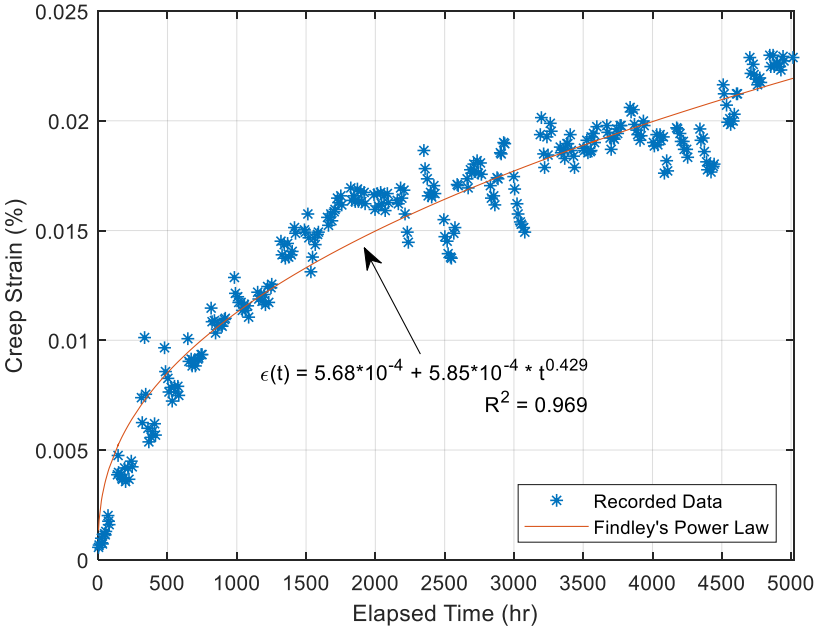

Figure 45: Comparison of Recorded Creep Strain and Regression Model Prediction

As noted above and seen in Figure 41, the creep deflections tended to exhibit significant variability after an elapsed time of around 2,250 hours, while maintaining a relatively constant

average value up to around 4,500 hours. As seen in Figures 42 and 43, the recorded OWL ambient relative humidity and temperature also experienced increased variability around these times. This variation is understandable as it corresponds with late spring / early summer where changes in temperature and humidity are to be expected. To examine their effects, the recorded ambient humidity and temperature after 1,500 hours were normalized relative to their value at 1,500 hours and plotted alongside normalized creep deflections in Figure 46 and 47 respectively. As can be seen, large spikes in temperature primarily, and humidity to a smaller extent, correspond with large drops in apparent creep deflection and vis-versa, suggesting a correlation exists. This is likely due to a differential in coefficient of thermal expansion between the concrete deck and FRP girder. This mismatch cases a curvature to form through the section during a temperature change leading to upward and downward deflection during increases and decreases in temperature, respectively. Although a similar curvature may exist as a result in differences in coefficient of moisture expansion, it is more likely that humidity changes accompany temperature changes and so do not have the same effect.

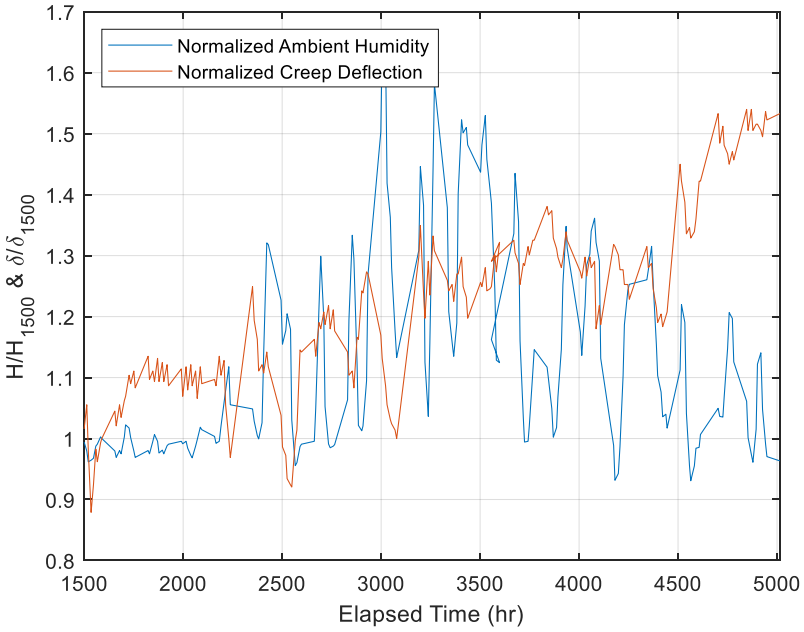

Figure 46: Variation in Creep and Humidity

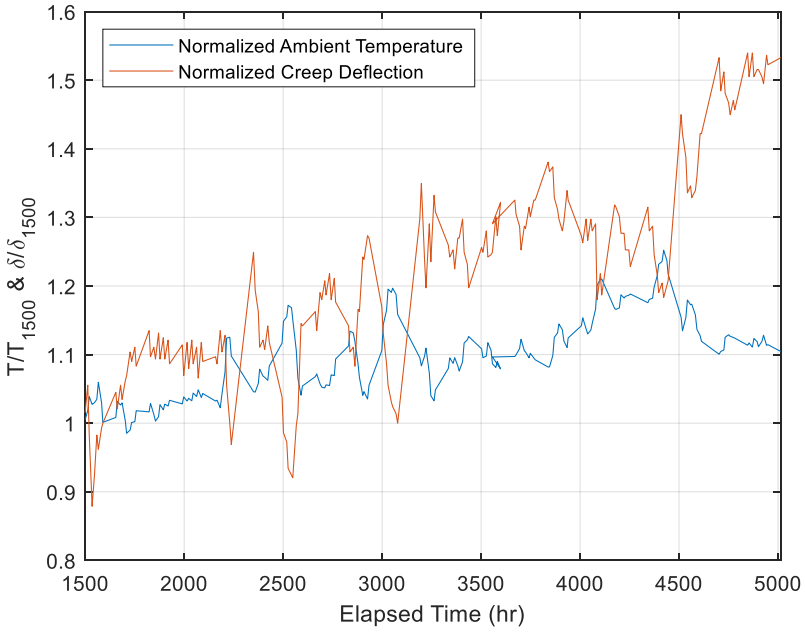

Figure 47: Variation in Creep and Temperature

The final recorded midspan creep after 215 days of elapsed time was 0.44 in. This leads to a ratio of midspan creep to instantaneous deflection of 37.3% and expected total deflection of 1.62 in. The total deflection determined as the average difference between height-of-deck from the floor at specimen ends and midspan was 2.06 in., which is 0.44 in. greater than 1.62 inches. However, as shown in Figure 40, the predicted deflection due to shrinkage of concrete at 215 days is significant, around 0.65 in. Although the girder was fully supported along its length until the start of the creep test, the girder was placed on simple supports at the beginning of the test, 61 days after deck casting, Figure 40 shows that locked-in shrinkage strains could have caused an additional, immediate deflection of up to around 0.47 in. 61 days after casting that was not have been measured during creep testing. Additional shrinkage deflection occurring over the course of the test is captured as part of the measured creep deflection, but this initial estimated shrinkage deflection of 0.47 in. is very close to the 0.44 inch discrepancy. Also, during the course of testing it was revealed that during manufacture, the specimen had experienced numerous manufacturing problems ranging from severe web delamination requiring repair infusion to poor concrete mix quality. Although it is not possible to precisely measure their effects, these manufacturing defects could have affected the specimen's overall stiffness and contributed to excess deflection.

3.4 Conclusions and Future Work

As only a single girder specimen was tested in creep which contained various manufacturing defects, the conclusions that can be drawn from this testing are somewhat limited. However they are still useful in describing the general behavior of UTC-1 in creep and may also inform future

testing and design or help to explain the behavior of similar girders in the field. First, the recorded apparent creep deflection, as seen in Figures 41 and 44, varied logarithmically with time as is the case for the visco-elastic response of many materials. It can therefore be concluded that, with additional data, relatively simple models may be able to be developed to predict creep deflection of CT girders over time which could be used for design in the future. Additionally, as is apparent in Figure 47, ambient temperature changes affect apparent creep behavior significantly, causing large fluctuations in instantaneous no-load deflection.

Moving forward, additional creep testing and monitoring of longer-term deflections of in-service bridges would be valuable to solidify the conclusions drawn in this work and to further develop models that can be used to aid in design. Greater numbers of specimens with varying details (span length, layup, etc.) should be tested, and the data used to develop more general models that designers can use to estimate creep deflections. These specimens should also be tested for longer periods to better evaluate their long-term behavior. This could also help to characterize girder temperature-dependence, as these specimens could be subjected to both cold- and warm-weather conditions which occur throughout the year.

4 Full-Scale Double CT-Girder Strength Testing

A full scale double CT girder was tested under service-level, strength-level, and ultimate-level loads to evaluate its live-load behavior at multiple loading levels. This girder, denoted "UTC-1", was designed to emulate an individual girder from a double-T CT girder module. UTC-1 was the same girder creep tested in the previous section, which included a full 12 in. depth cast-in-place deck and integral, monolithic end diaphragms. A second girder, UTC-2, was constructed to be nominally identical, with the exception that the deck consisted of two layers: a 4 in. cast-in-place slab with an additional 8 in. precast slab placed on top. It was tested as UTC-1 had been, but failed prematurely due to manufacturing flaws in the upper portion of the web and flange.

4.1 Instrumentation and Test Protocol

4.1.1 Test Set-Up

Figures 48 and 49 show the general configuration in side- and end-elevation views of strength tests at each of the three load-levels. The girder was simply supported on either end by a 5 in. reinforced bearing pad atop a large concrete support block. Loading was applied in a 4-point bend configuration with a servo-hydraulic actuator reacting against a spreader beam (referred to as the "10-ton beam" in Figures 48 and 49) which in-turn reacted against two smaller sections that spread the load across the full girder width. This configuration provided a 14 ft section of constant moment at the center of each girder and 20 ft of linearly varying moment at either end. Figure 50 shows a photograph of UTC-1 in testing configuration.

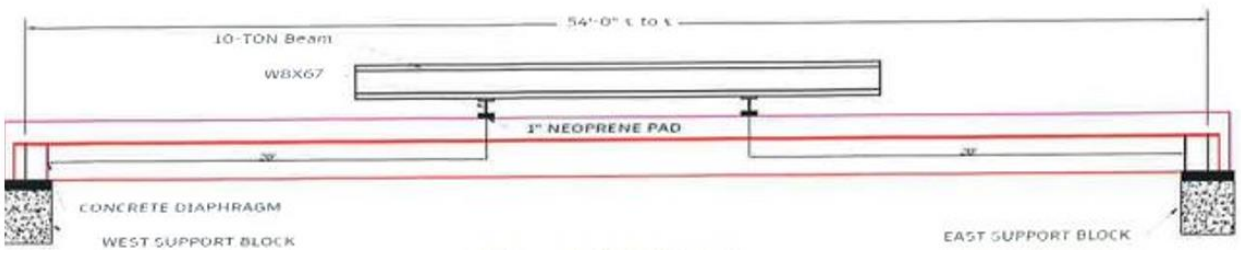

Figure 48: Test Configuration – Side Elevation

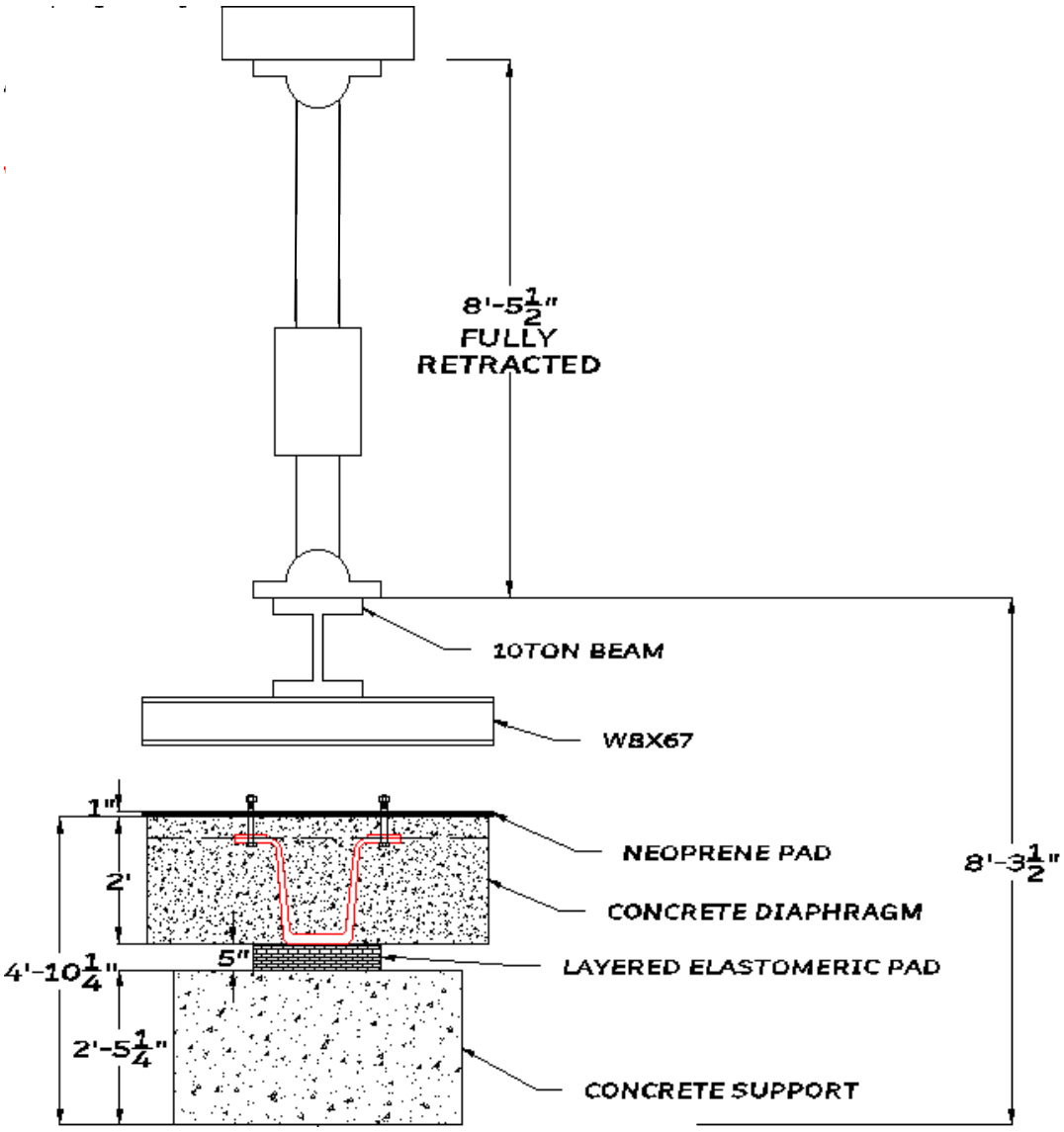

Figure 49: Test Configuration – End Elevation

Figure 50: UTC-1 in Test Configuration

4.1.2 Instrumentation

The girder was provided with a wide range of instrumentation to examine its response to loading. Displacement was measured both by an internal linear variable differential transformer (LVDT) within the actuator providing load, as well as string potentiometers applied to the girder bottom at midspan. A 450 kip capacity load cell, mounted in-line with the load from the actuator, measured applied load. Separate LVDTs applied to the inside and outside faces of the end diaphragms measured displacement at the supports to correct for compression of the bearing pads. These, along with separate inclinometers, measured the rotation of the girder ends during loading. Separate LVDTs were mounted to the deck at either end to measure relative slip between the girder and deck to assess shear connector performance. Resistance foil strain gage rosettes were applied to the girder through its depth at sections 0.5 ft and 8 ft from either support to monitor shear strains through the girder's web. Additionally, uniaxial foil resistance strain gauges were applied through the girder's depth at midspan to track longitudinal strains.

4.1.3 Test Protocol

The girder was tested at three, increasing load-levels to evaluate its behavior under high load levels. During the service-level test, load was ramped up to the girder's AASHTO [4] Service I moment, 8640 in-kip, with this loading applied three times to ensure repeatability. During the strength-level test, it was loaded to its AASHTO Strength I moment, 15,660 in-kip, which was

repeated twice. Finally, during the failure test, the girder was loaded monotonically to failure, defined as a sudden loss of load-carrying capacity or large deflection increases under small marginal load.

4.2 UTC – 1

As noted earlier, UTC-1 was the girder tested previously in creep and so included that loading history as well as the unknown repair mentioned in Section 3. As the location and type of repair were unknown, their effects on behavior cannot be definitively identified. However, it is suspected that they contributed to the girder's inability to reach full moment capacity (as discussed later).

To account for long-term effects, strain in the bottom flange due to uniform shrinkage of the full-depth cast-in-place deck was determined and subtracted from the bottom fiber ultimate strain. To find this, shrinkage deflection was assumed at midspan to equal the total deflection measured at the end of creep testing less the creep deflection and this value inserted into Equation 5 which was solved for the curvature ϕ. This could then be inserted into Equation 3 to solve for ε_{sh}. The strain at the section bottom could then be found by adding the observable bending and axial strains and subtracting the shrinkage strain, in much the same way as a thermo-mechanical analysis would be performed and could be subtracted from the bottom fiber's ultimate tensile strain ε_{1t} to reduce the maximum computed moment resistance. This is outlined in Equations 9 through 12 in which A_c is the cross-sectional area of the concrete deck, A_T is the area of the composite girder determined by transformed sections, and y is the vertical coordinate.

$$\varepsilon_a + \varepsilon_\phi = \varepsilon_{sh} + \varepsilon_\sigma \qquad \text{Equation 9}$$

$$\varepsilon_a = \frac{1}{A}\int \varepsilon_{sh} dA = \frac{\varepsilon_{sh} A_c}{A_T} \qquad \text{Equation 10}$$

$$\varepsilon_\sigma(y = 0) = \phi * (\bar{y} - y) + \varepsilon_a - \varepsilon_{sh}(y) \qquad \text{Equation 11}$$

$$\varepsilon_{1t-Reduced} = \varepsilon_{1t} - \varepsilon_\sigma(y = 0) \qquad \text{Equation 12}$$

4.2.1 Service and Strength Tests

Service and strength level tests were performed on UTC-1 on December 1, 2021 in the OWL. The specimen withstood this loading without apparent signs of distress or loss of performance. Figure 51 presents the girder's load-displacement behavior which shows a maximum displacement under strength load of 1/64 the span length. It also shows very little difference between the upward and downward load ramps, indicating little or no incurred damage. Figure 52 presents the slip recorded between the FRP girder and deck. The very small relative movement

indicates that the ridged FRP shear connection is working to provide composite action along the entire length of the girder.

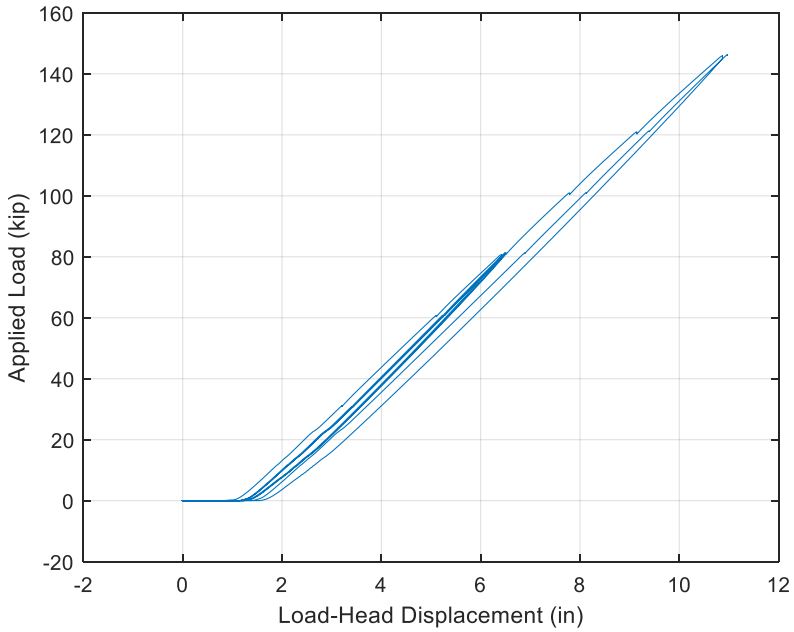

Figure 51: UTC-1 Service & Strength Load-Displacement Behavior

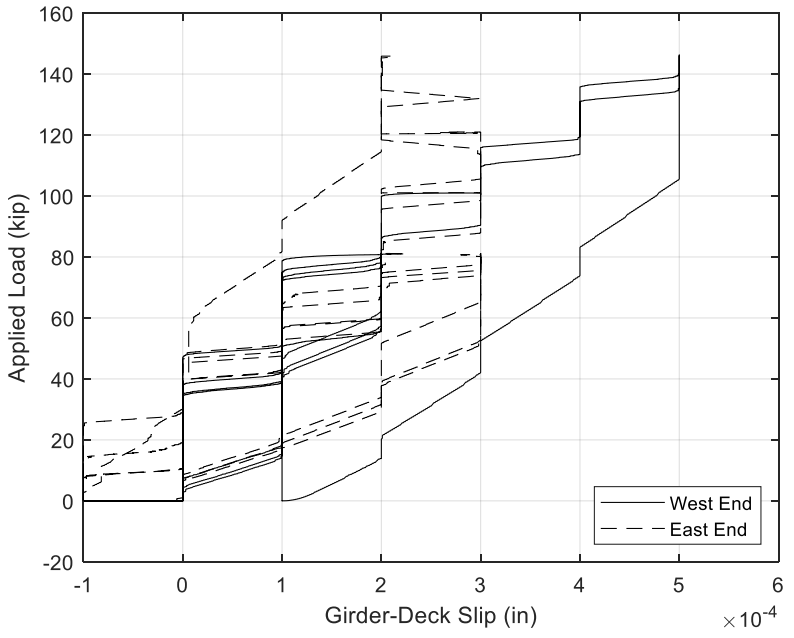

Figure 52: UTC-1 Service & Strength Deck Slip

The strains recorded through the girder's depth throughout testing display a combination of expected and unexpected behavior. Figures 53 and 54 show the longitudinal strains recorded at midspan on the girder's North and South faces, respectively. The longitudinal strains on the North side display the expected behavior: linear increase in strain with load, with magnitude proportional to distance to the neutral axis (which is assumed to lie within the concrete deck as all longitudinal strains recorded on the girder were tensile). Strains recorded on the South side also increase linearly with load. However, in this case the strains are not proportional to the distance to the neutral axis, with the gage at the bottom of the web reading higher strains than the bottom flange. This seems to violate Euler-Bernoulli beam theory assumptions, bringing these results into question. However, this violation persists in shear strains recorded at 6 in. and 8 ft from the supports, as seen respectively in Figures 55 and 56, which are higher further away from the neutral axis, also violating standard beam theory. The reasons for these deviations are not immediately apparent. One possibility is that the unknown girder repairs significantly impacted the relative distribution of shears to each web.

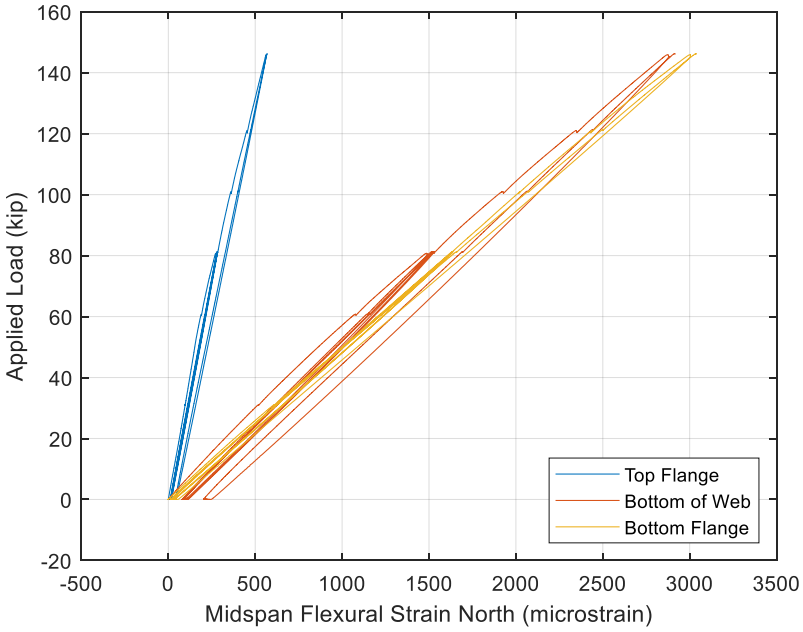

Figure 53: UTC-1 Service & Strength North Face Longitudinal Strain

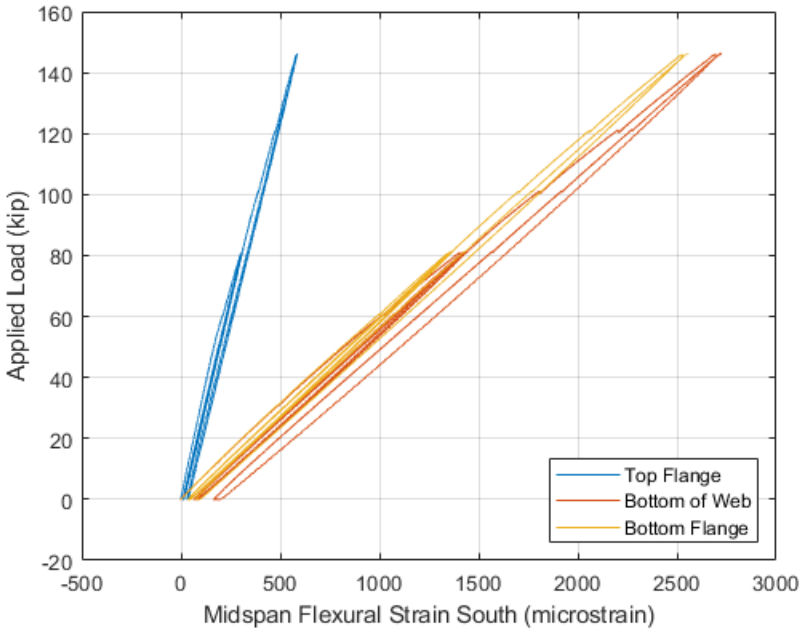

Figure 54: UTC-1 Service & Strength South Face Longitudinal Strain

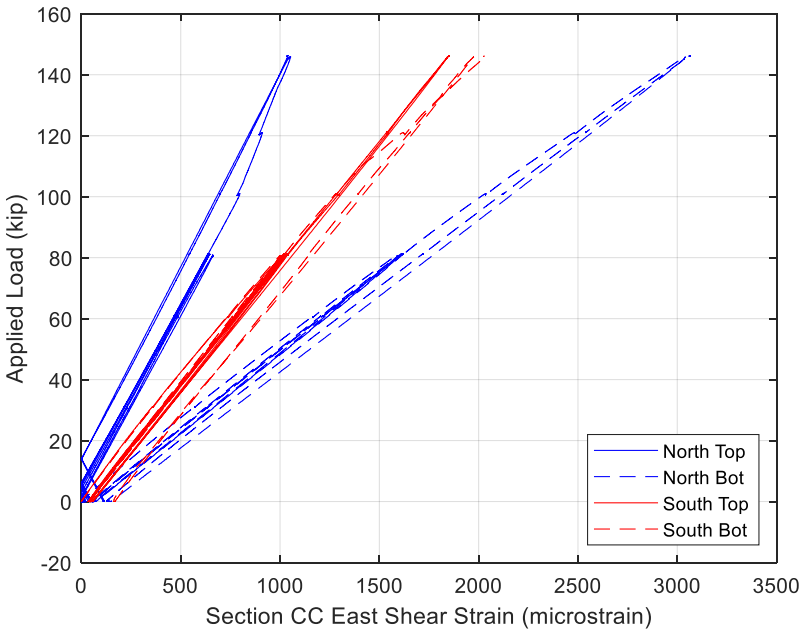

Figure 55: UTC-1 Service & Strength Shear Strain 6 in. from Support

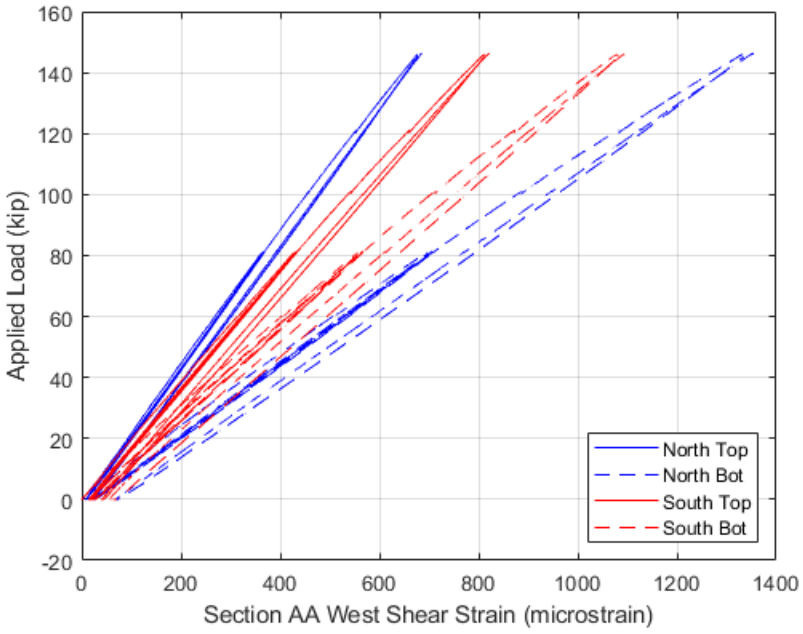

Figure 56: UTC-1 Service & Strength Shear Strain 8 ft from Support

4.2.2 Failure Test

Failure testing was performed in December 2, 2021 in the OWL. Like during its service and strength tests, the girder displaced essentially linearly with load up to failure, as seen in Figure 57. After three initial, smaller load ramps, the girder was loaded monotonically to failure. Failure occurred at an applied load of 325 kip, corresponding to a moment of 35,100 in-kip, a moment 124% greater than the moment caused by AASHTO [4] Strength I loading. At this point, the bottom flange appeared to experience tensile rupture causing the girder to collapse. However, this moment was significantly smaller than the expected moment capacity of 52,300 in-kip based on bottom-flange tensile rupture. This theoretical capacity was determined using a nonlinear moment-curvature analysis with the ultimate tensile strain of the carbon in the bottom flange (less the locked-in dead-load strain and strain due to shrinkage) as a failure indicator. This nonlinear moment-curvature analysis was conducted using layered analysis, where the FRP was assumed to be linearly elastic and the concrete to obey the Hognestad model [12] in compression. This is the same method used for design of the FRP girders in practice [13, 14]. It is possible that the girder's repair could have affected its ultimate moment capacity, but without more specific information regarding the repair this is speculation.

It should be noted that at a load of around 300 kip, there was a disturbance in the load-displacement results that can be seen in Figure 57 as two "saw-tooth" bumps. This also occurs in many other data sets. This could help describe some of the behavior seen afterward. Similar to the service and strength tests, small relative displacements recorded between the FRP girder and deck

indicated that the ridged FRP connection was effective in ensuring composite action throughout the course of loading. These can be seen in Figure 58.

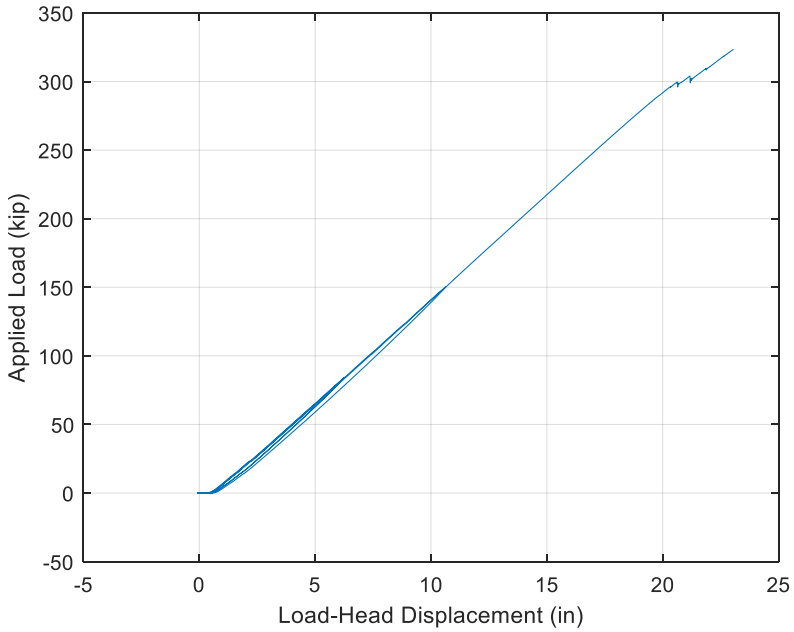

Figure 57: UTC-1 Ultimate Load-Displacement Behaviors

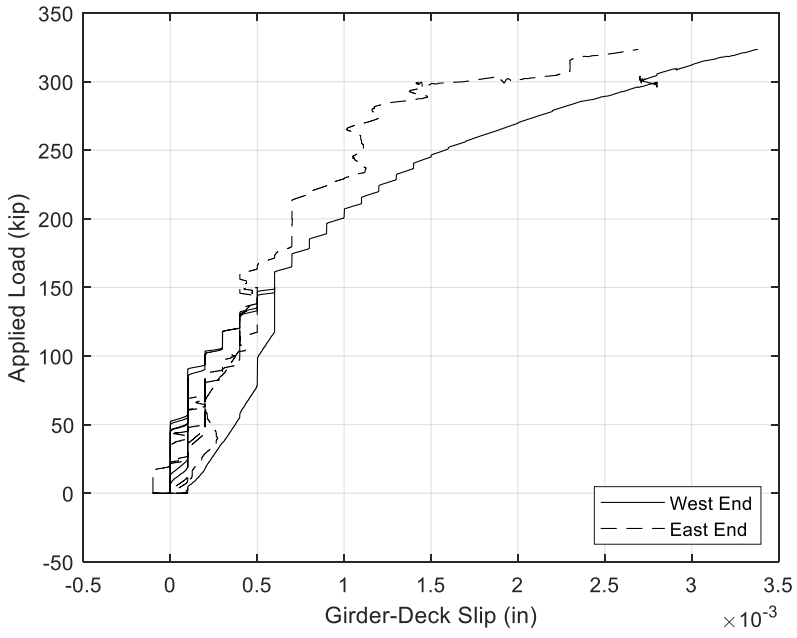

Figure 58: UTC-1 Ultimate Deck Slip

The longitudinal strains recorded during failure testing indicate expected flexural behavior when each side of the girder is examined separately. Figures 59 and 60 show that strains increase linearly with load up to loads close to failure, and that strains are higher at locations further from the neutral axis (again assumed to lie in the concrete deck). However, the strains recorded at the North side of the bottom flange are significantly higher than those recorded on the South side, where they should be equal. This suggests that the load path from the deck to the bottom flange is not evenly distributed through both webs, resulting in a strain gradient across the width of the bottom flange.

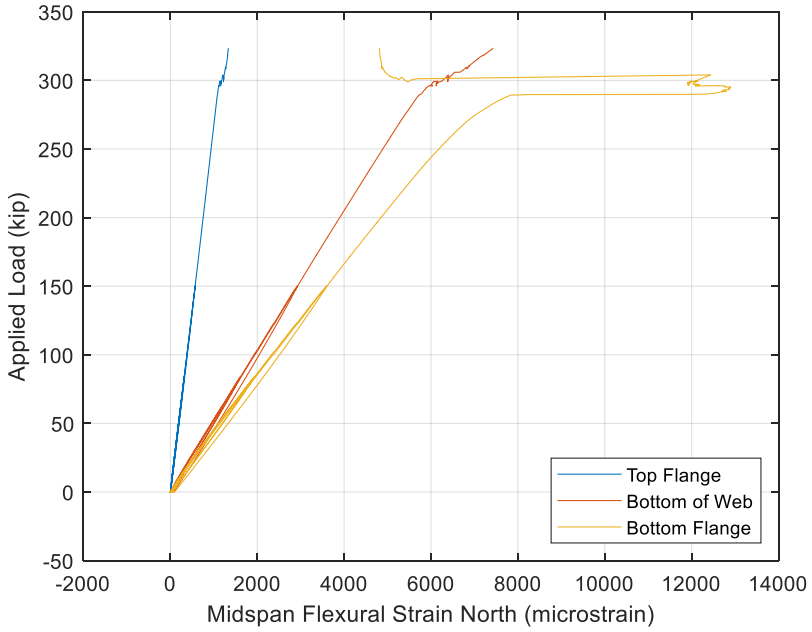

Figure 59: UTC-1 Ultimate North Longitudinal Strain

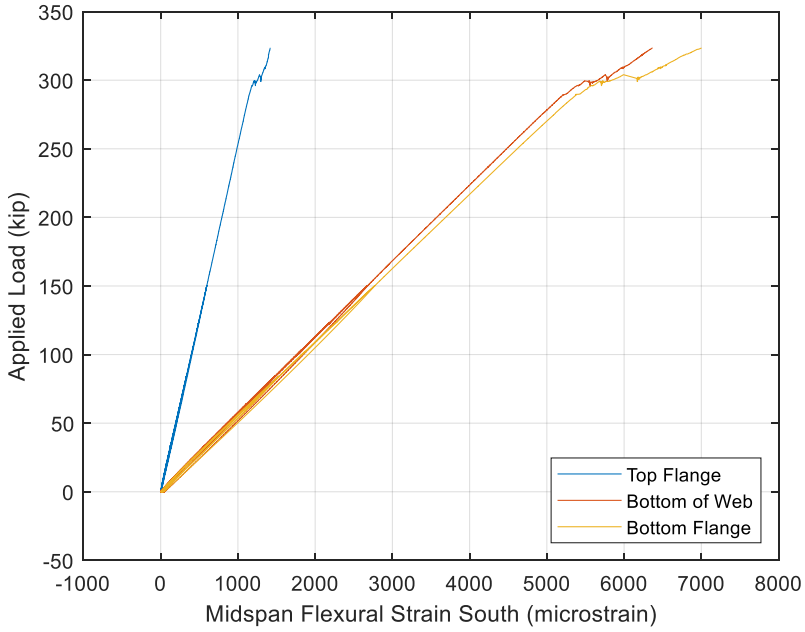

Figure 60: UTC-1 Ultimate South Longitudinal Strain

As was mentioned above, the data show that some sort of disturbance to the girder's behavior occurred at a load of around 300 kip. This can be seen most clearly in Figure 61, which shows shear strain 6 in from the East support. As can be seen, the girder experienced a very significant jump in shear strain at this section at around 300 kip, which may indicate a partial shear failure. This could help to explain the girder's unexpected behavior past 300 kip, as well as its inability to reach the expected failure moment. For reference, plots of the other recorded shear strains are provided in Figures 62-64. It should be noted that the shear strains recorded 8 ft from the West support displayed expected behavior with higher strains nearer to the neutral axis. At all other locations, the opposite of this was observed.

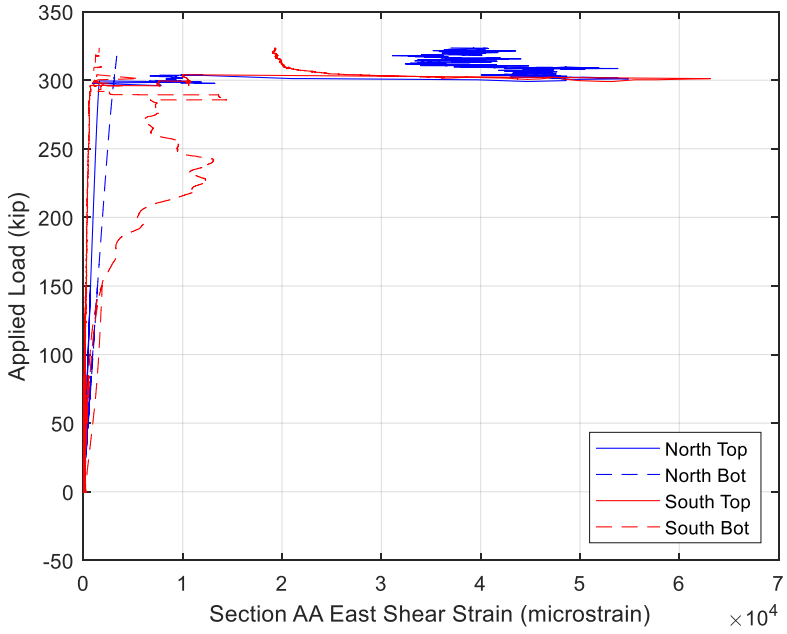

Figure 61: UTC-1 Ultimate Shear Strain 6 in. from East Support

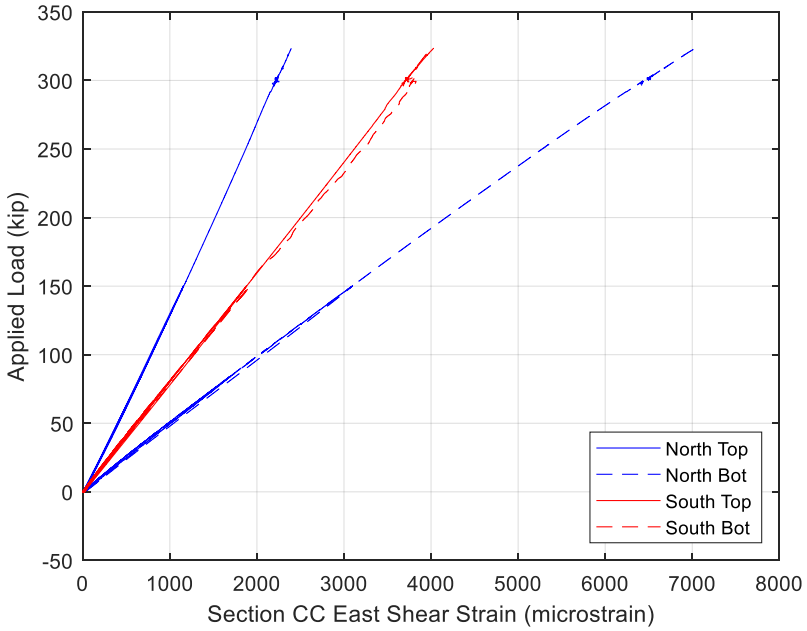

Figure 62: UTC-1 Ultimate Shear Strain 8 ft from East Support

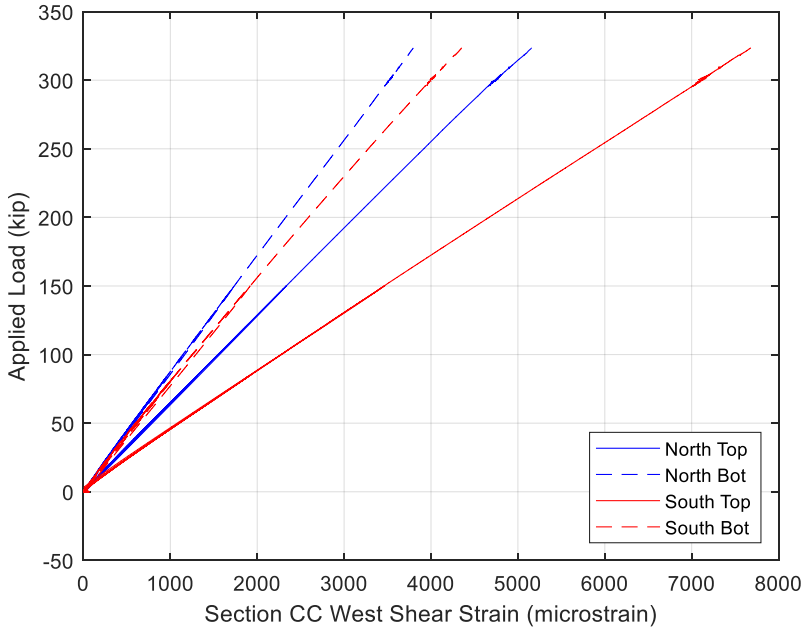

Figure 63: UTC-1 Ultimate Shear Strain 8 ft from West Support

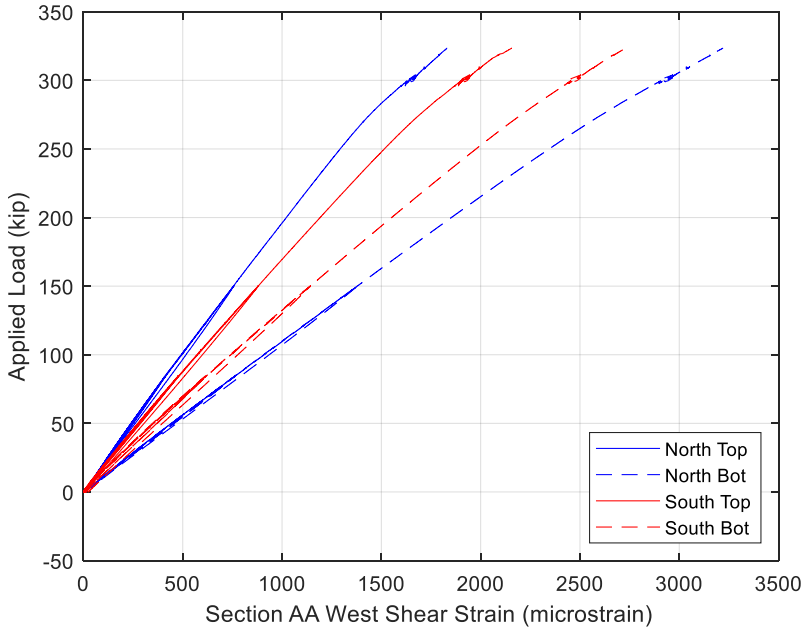

Figure 64: UTC-1 Ultimate Shear Strain 6 in. from West Support

4.3 UTC- 2

The second girder specimen, “UTC-2” was tested in a manner similar to UTC-1. However, this specimen was constructed with a two-layer deck – a bottom, 4 in. precast slab layer with an 8 in. cast-in-place top layer. This provided the opportunity to test the specimen under simulated non-composite construction loading during placement of the deck top layer as well as composite service, strength, and failure loading.

4.3.1 Construction Loads Test

Prior to pouring its second deck layer, UTC-2 was tested in a 4-point bending configuration on July 7, 2021. Figure 65 shows the loading sequence including all load ramps, plateaus, and repetitions. The first repeated sequence, during which 23.3 kip of load was applied, generated an internal moment at midspan equivalent to that of dead load of the 8 in. of wet concrete, simulating the non-composite construction dead load. The second sequence was also repeated twice, wherein the 50.5 kip applied load generated an internal moment at midspan equivalent to the previous modified dead load in addition to an assumed construction live load.

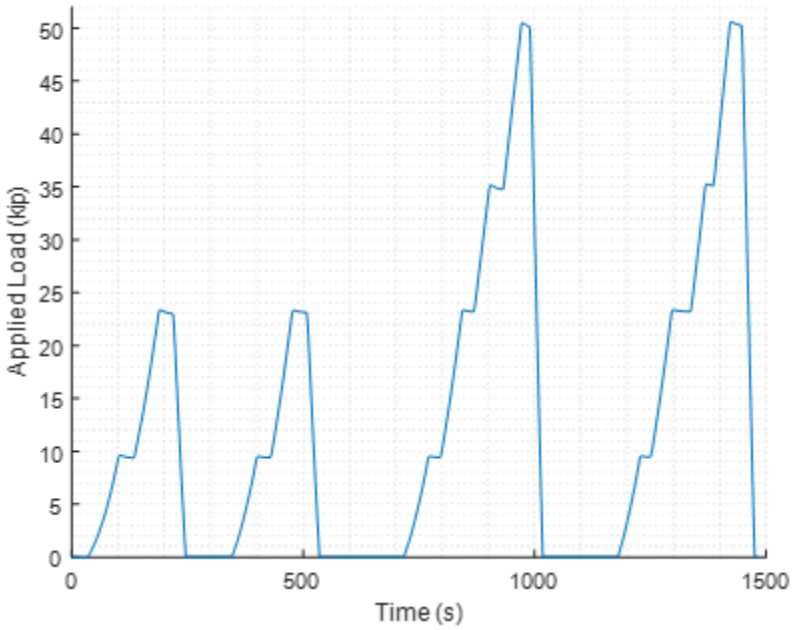

Figure 65: UTC-2 Construction Loads Test Sequence

As expected, the specimen responded linearly to the applied loading during the construction load sequence as can be seen in Figure 66. It should be noted that, after the first load ramp, a small amount of permanent, non-recoverable deflection was measured. This can be neglected as it is likely due to minor movement of the specimen and test set-up, as witnessed by the negligible effect on overall stiffness. A best-fit line was fit to the loading phase for each of the four sequences, allowing a slope (equivalent to the specimen’s bending stiffness) to be calculated.

The results of this summarized in Table 4. Comparison with a theoretically determined stiffness the specimen behaved 20.8% stiffer than anticipated.

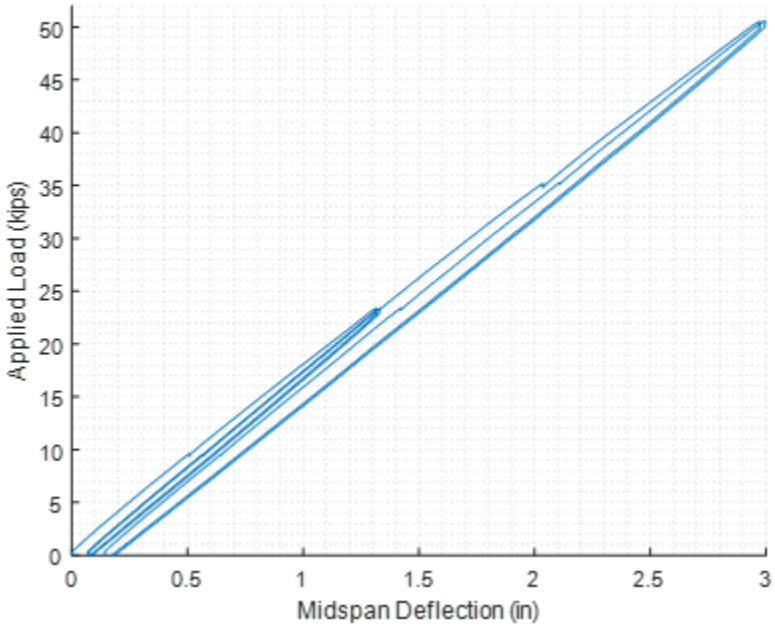

Figure 66: UTC-2 Applied Load vs. Deflection at Midspan

Table 4: Estimated Stiffness from Construction Load Test

Load Phase (kip)	Repetition	Slope (kip/in)
23.3	1	17.5
	2	18.3
50.5	1	17.4
	2	17.6
	Average	17.7
	COV	2.15%

Figure 67 shows the longitudinal strains recorded through the specimen's depth at midspan. As anticipated, strains are linearly proportional to the applied load and to the distance from the neutral axis. As is evident from the negative strains recorded in the top flange, the neutral axis of the section was located below the 4 in. precast concrete deck. This also coincided with expectations. The LVDTs applied to measure slip between the FRP girder and the 4 in. precast concrete deck did not record any significant displacement. This indicates full effective composite action.

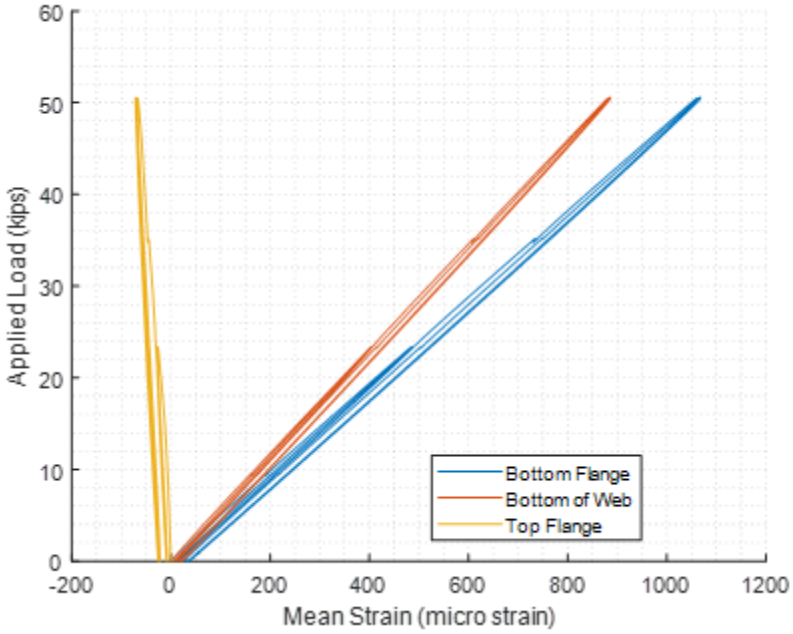

Figure 67: UTC-2 Applied Load vs. Midspan Strain

4.3.2 Service, Strength and Failure Tests

The 8 in. cast-in-place deck layer was poured on July 20, 2021. Further testing resumed on August 18, 2021, after the concrete had cured sufficiently. Applied load sequences and load-deflection data are presented in Figures 68 and 69. The 81.1 kip service load sequence was applied once, and the 146 kip Strength I load sequence was repeated twice. After Strength I testing, the intention was to load the specimen to failure. However, after reaching a load of approximately 255 kips, multiple loud popping sounds emanated from the specimen, and it was thought that failure had been reached at a load of 264 kip. Upon inspection of the specimen, it was determined that a second ramp to failure could be attempted. Final destructive failure was reached at a load of 253 kip.

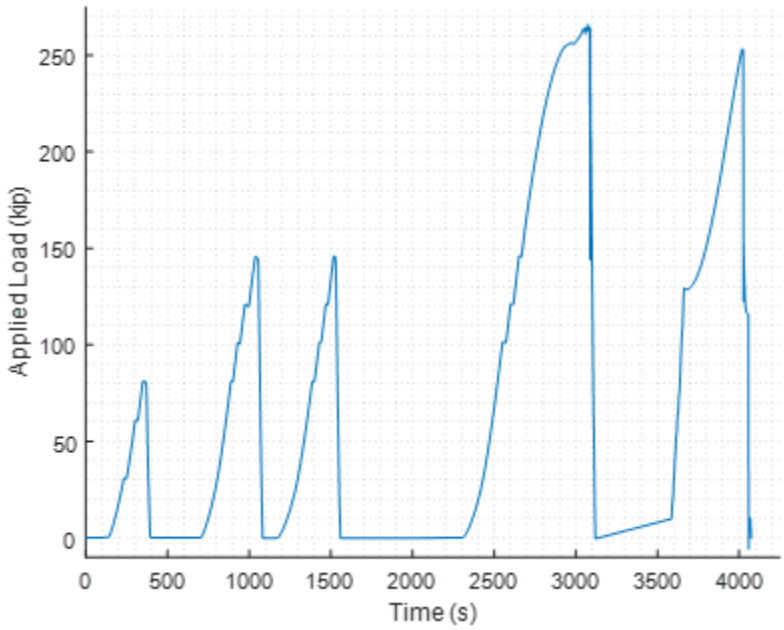

Figure 68: UTC-2 Service, Strength I, and Failure Load Sequencing

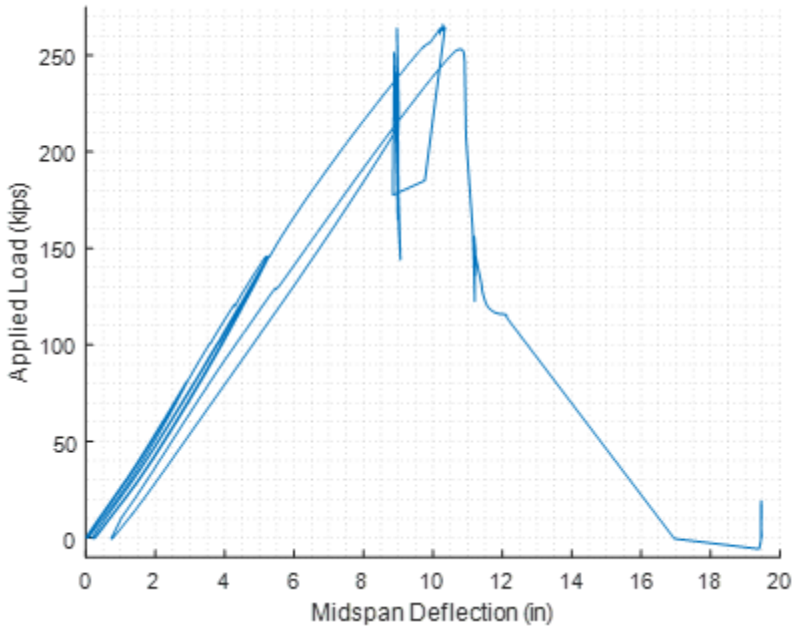

Figure 69: UTC-2 Applied Load vs. Deflection at Midspan

A best fit line was applied to the loading phase for each of the five sequences, and an observed stiffness was calculated based on the slopes. The results are summarized in Table 5. It

is worth noting that the relatively linear response of the specimen was maintained after the first failure (post 264 kips).

Table 5: Estimated Stiffness from Service, Strength I, and Failure Tests

Load Phase (kip)	Repetition	Slope (kip/in)
81.1	1	27.6
146	1	28.7
	2	28.6
264	1	26.6
255	1	25.0
	Average	27.3
	COV	5.63%

4.3.3 Results and Discussion

Figure 70 compares the specimen before and after failure 264 kips. The specimen failed by local buckling at the web-top flange transition radius. Video recordings verified this failure. This was not an anticipated failure mode, so the top flange radius was not investigated during inspection between the two failure test attempts. The specimen experienced around 0.75 in. of permanent defection after failure as measured by a string potentiometer. A secondary failure occurred upon reaching 253 kips as shown in Figure 71**.** The picture was taken after removing the outermost black carbon veil. The following was observed after failure and inspection:

- Buckling of the webs at midspan
- Delamination of the web face sheets from the foam core at different locations around midspan
- Disassociation of the webs from the top flanges at midspan
- Excessive concrete deck cracks, but no crushing failure
- No apparent damage to the bottom flange

Different cuts were made after the second failure for further inspection. The left picture in Figure 72 shows an example of the results of top flange radius failure. This failure was exacerbated after loading to failure the second time, wherein the web layers delaminated from the top flange. The severity of this delamination was most apparent at midspan where the top flange and the webs disassociated completely. However, moving closer to the end diaphragms the severity of the delamination decreased.

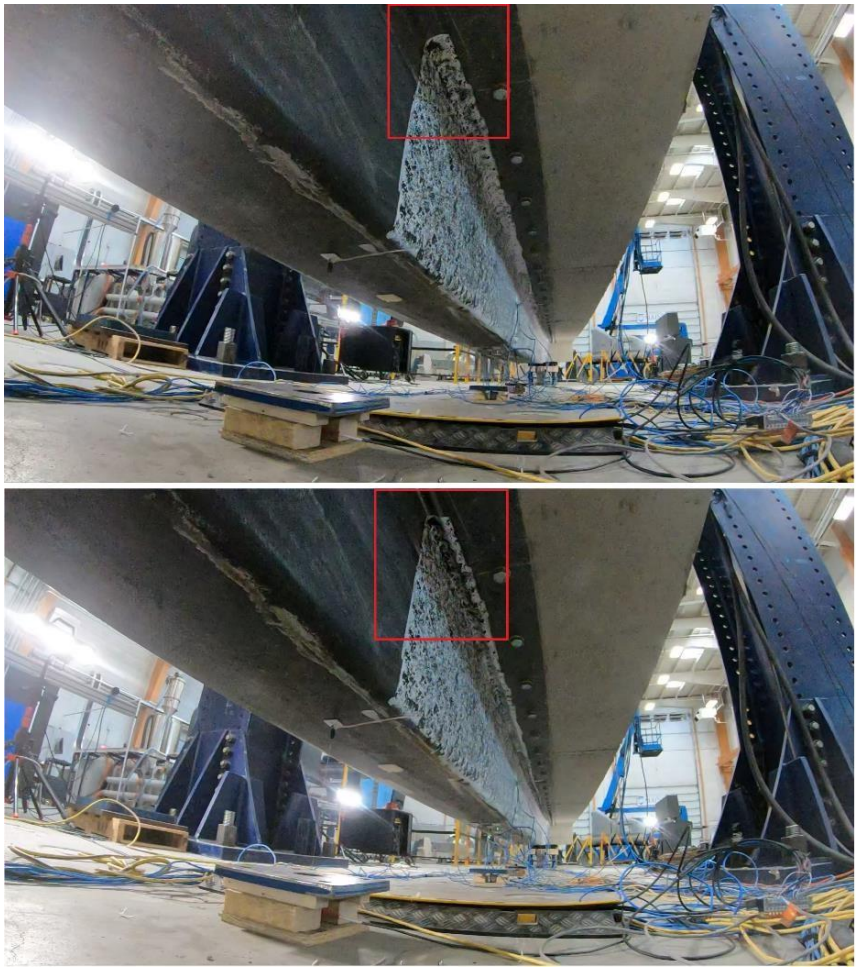

Figure 70: Before (Top) and after (Bottom) Pictures of Failure at 264 kips

Figure 71: UTC-2 After the 253 kip Failure Load

Figure 72: Top Flange Radius Buckling (Left) and Delamination (Right)

The failure of the transition area between the top flange and the webs was the most significant result of testing UTC-2. Both UTC-1 and UTC-2, as well as other, commercial girders were fabricated with the assumption that a 2 in. overlap between layers of the web and layers of the top flange was sufficient to transfer the stresses. However, this test has shown that a higher level of conservatism should be adopted in the design of this transition area. This failure did not allow for loading the specimen up to its theoretical moment failure or for achieving the ultimate tensile strain in the bottom flange.

4.4 Conclusions and Future Work

A full-scale, previously creep tested CT girder was tested under service, strength, and ultimate loading to examine its behavior in bending. Although it was not able to reach its predicted ultimate capacity, the results of testing allow some conclusions to be drawn. First, the lack of significant slip between the girder and deck confirms that its sinusoidally ridged profile acts as an effective shear interlock mechanism, providing, effectively, full composite action up to the point of failure. Second, the girder's apparent violation of plane-section assumptions leads to the conclusion that the girder's behavior is significantly affected by the presence of manufacturing defects. This is further evidenced by its inability to reach its expected flexural failure capacity, which is likely a direct result of its manufacturing defect. Finally, the girder's linear behavior to failure confirms this design assumption, greatly simplifying potentially difficult nonlinear design procedures.

Moving forward, it is vital that additional full-scale girder specimens be tested to failure. These additional tests will allow a greater confidence in our understanding of their behavior. These additional specimens must be manufactured without defects for a true characterization of their behavior. In addition, girders should be tested in fatigue to assess their long-term cyclic behavior and ability for long-term durability.

5 References

1. Davids, W.G., Guzzi, D., & Schanck, A.P. (2022). Development and experimental assessment of friction-type shear connectors for FRP bridge girders with composite concrete decks. *Materials*. 15(9):3014.

2. Guzzi, D. (2019). *Milestone 29: Final Joint Testing*. University of Maine, Orono ME.

3. Schanck, A. (2020). *Milestone 25: Develop additional joints concepts, manufacture scale test artices, and perform static and fatigue tests.* University of Maine, Orono ME.

4. AASHTO. (2012). *AASHTO LRFD Bridge Design Specifications*. American Association of State Highway and Transportation Officials, Washington DC.

5. ASTM International. (2020).*C39/C39M-20 Standard Test Method for Compressive Strength of Cylindrical Concrete Specimens*. West Conshohocken, PA.

6. Scott, D.W., Lai, J.S., & Zureick, A.H. (1995). Creep behavior of fiber-reinforced polymeric composites: a review of the technical literature. *Journal of Reinforced Plastcs and Composites.* 141995): 588-617.

7. Ascione, L., Berardi, V.P., & D'Aponte, A. (2012). Creep phenomena in FRP materials. *Mechanics Research Communications*. 43(2012): 15-21.

8. Bazant, Z.P. (1972). Prediction of concrete creep effects using age-adjusted effective modulus method. *Journal of the American Concrete Institute*. 69(1972): 212-217

9. AASHTO. (2012). *LRFD Guide Specifications for Design of Concrete-Filled FRP Tubes for Flexural and Axial Members*. American Association of State Highway and Transportation Officials, Washington DC.

10. Videla, C.C. & Carreira, D.J. (2008). *Guide for Modeling and Calculating Shrinkage and Creep in Hardened Concrete*. American Concrete Institute, Farmington Hills, MI.

11. Findley, W.N. (1987). 26-year creep and recovery of poly (vinyl chloride) and polyethelene. *Polymer Engineering and Science*. 27(8):582-585.

12. Hognestad, E. (1951). *A Study of Combined Bending and Axial Load in Reinforced Concrete Members, Bulletin Series No 399.* THe University of Illinois, Urbana, IL.

13. Davids, W.G., Diba, A., Dagher, H.J., Guzzi, D., & Schanck, A.P. (2022). Development, assessment and implementation of a novel FRP composite girder bridge. *Construction and Building Materials*. 340(2022):127818.

14. AIT. (2019). *Calculation Package for Grist Mill Bridge No. 2334 Over Soudabscook Stream Hampden, Maine.* Advanced Infrastructure Technologies, Brewer, ME.

A.1 Shear Flow and Fatigue Loading Calculations

Double CT Girder Fatigue- Loading Calculations

Bridge Details

$L := 53\ ft$	Span Length
$t_{ws} := 0\ in$	Wearing Surface Thickness
$n_{stud} := 2$	Number of Studs per Row
$I_{transPre} := (8.44210 \cdot 10^3)\ in^4$	Precomposite Transformed Moment of Inertia
$Q_{Pre} := 418.18\ in^3$	Precomposite Transformed 1st Moment of Area to Shear Plane
$I_{transPost} := (1.7546 \cdot 10^4)\ in^4$	Postcomposite Transformed Moment of Inertia
$Q_{Post} := 697.88\ in^3$	Postcomposite Transformed 1st Moment of Area to Shear Plane

Dead Loading

$V_{Pre} := 24.53\ kip$	Precomposite Dead Load Shear
$V_{Barrier} := 2.36\ kip$	Shear from Barriers (Estimated)
$V_{ws} := 0\ kip$	Wearing Surface Shear (Composite Wearing Surface)

Strength I Shear Loading

$\gamma_{LL} := 1.75 \quad IM := 1.33$ $\gamma_{DW} := 1.5 \quad \gamma_{DC} := 1.25$	Load and Impact Factors
$g_v := 0.5$	Shear Distribution Factor
$P_{front} := 8\ kip$ $P_{back} := 32\ kip$	Axle Loads
$s := 14\ ft$	Axle Spacing
$w_{lane} := 0.64\ \frac{kip}{ft}$	Lane Load
$V_{truck} := P_{back} \cdot \left(1 + \frac{L-s}{L}\right) + P_{front} \cdot \left(\frac{L-2 \cdot s}{L}\right) = 59.321\ kip$	Shear from Load Tuck
$V_{lane} := \frac{w_{lane} \cdot L}{2} = 16.96\ kip$	Shear from Lane Load
$V_{LL} := g_v \cdot (V_{truck} \cdot IM + V_{lane}) = 47.928\ kip$	Live Load Shear
$V_u := \gamma_{DW} \cdot V_{ws} + \gamma_{DC} \cdot V_{Barrier} + \gamma_{LL} \cdot V_{LL} = 86.825\ kip$	Postcomposite Factored Shear

$V_{uPre} := \gamma_{DC} \cdot V_{Pre} = 30.663\ kip$ Precomposite Factored Shear

$q_u := \frac{V_u \cdot Q_{Post}}{I_{transPost} \cdot n_{stud}} + \frac{V_{uPre} \cdot Q_{Pre}}{I_{transPre} \cdot n_{stud}} = 2.486\ \frac{kip}{in}$ Factored Shear Flow

Fatigue I Shear Loading

$\gamma_{LL} := 1.75 \quad IM := 1.15$
$\gamma_{DW} := 1.0 \quad \gamma_{DC} := 1.0$ Load and Impact Factors

$g_v := 0.5$ Shear Distribution Factor

$P := 32\ kip$ Fatigue Truck Axle Load
$s := 30\ ft$ Fatigue Truck Axle Spacing
$a := 0\ ft$
$b := L - (a + s) = 23\ ft$

$V_{truck} := \frac{P}{L} \cdot (L - a + b) = 45.887\ kip$ Fatigue Truck Shear

$\gamma V_{Fatigue} := \gamma_{LL} \cdot IM \cdot V_{truck} \cdot g_v = 46.174\ kip$ Factored Fatigue Shear

$\gamma V_{DeadPre} := \gamma_{DC} \cdot V_{Pre}$

$\gamma V_{DeadPost} := \gamma_{DW} \cdot V_{ws} + \gamma_{DC} \cdot V_{Barrier} = 2.36\ kip$ Factored Dead Load Shear

$q_{Live} := \frac{\gamma V_{Fatigue} \cdot Q_{Post}}{I_{transPost} \cdot n_{stud}} = 0.918\ \frac{kip}{in}$ Factored Live Load Shear Flow

$q_{DeadPre} := \frac{\gamma V_{DeadPre} \cdot Q_{Pre}}{I_{transPre} \cdot n_{stud}} = 0.608\ \frac{kip}{in}$ Factored Dead Load Shear Flow

$q_{DeadPost} := \frac{\gamma V_{DeadPost} \cdot Q_{Post}}{I_{transPost} \cdot n_{stud}} = 0.047\ \frac{kip}{in}$

$q_{Dead} := q_{DeadPre} + q_{DeadPost} = 0.654\ \frac{kip}{in}$

Fatigue Loads for Ridged Push-Out Specimens

$n := 2$	Number of GFRP Plates
$l := 22\ in$	Length of Contact between Plates and Concrete
$P_{range} := n \cdot l \cdot q_{Live} = 40.403\ kip$	Load Range to Apply Fatigue Live Load Shear Flow
$P_{dead} := n \cdot l \cdot (q_{DeadPre} + q_{DeadPost}) = 28.797\ kip$	Load to Apply Fatigue Dead Load Shear Flow
$P_{min} := \max(P_{dead}, 10\ kip) = 28.797\ kip$	Minimum Applied Test Load
$P_{max} := P_{min} + P_{range} = 69.201\ kip$	Maximum Applied Test Load
$P_{mid} := \frac{P_{range}}{2} + P_{min} = 48.999\ kip$	Average Applied Test Load

$q_u = 2.49\ \frac{kip}{in}$

$q_{Live} = 0.92\ \frac{kip}{in}$

$q_{Dead} = 0.65\ \frac{kip}{in}$

$P_{min} = 28.8\ kip$

$P_{max} = 69.2\ kip$

$P_{mid} = 49\ kip$

A.2 Concrete Cylinder Test Reports from the Hampden Grist Mill Bridge Deck Pour

S.W.COLE ENGINEERING, INC.

Report of Concrete Compressive Strength

ASTM C-31/ C-39 / C-1231

Project Name: Hampden ME - Grist Mill Bridge - Concrete Testing

Project Number: 20-1142

Report Date: 1/5/2021

Client: T. Buck Construction, Inc.

Client Contract Number:

General Contractor:

Concrete Supplier: O.J. Folsom

PLACEMENT INFORMATION

Date Cast: 12/8/2020 **Time Cast:** 12:06 **Date Received:** 12/9/2020

Placement Location: BRIDGE DECK

Placement Method: Pump

Placement Vol. (yd³): 115

Cylinders Made By: Brendan Auth

Aggregate Size (in): 3/4

INITIAL CURING CONDITIONS

Temperatures

Minimum (°F) 52 **Maximum (°F)** 66

DELIVERY INFORMATION

Admixtures: AIR / SUPER / 2% NCA

TEST RESULTS

Slump (in) (C-143):

Air Content (%) (C-231) 8.5

Air Temp (°F): 31

Conc. Temp (°F) (C-1064): 60

Load Number: 68

Mixer Number: 3

Ticket Number 4380

Cubic Yards: 10

Design (psi): 4000

Batch 10:43

Arrive 11:30

Depart 12:00

Cylinder Designation	Cylinder Weight (lbs)	Cylinder Diameter (in)	Cross Sectional Area(In)²	Date Of Test	Cure Type	Cap Type	Age (days)	Fracture Type	Load (kips)	Strength (psi)
939-30A	8.00	3.99	12.50	12/15/2020	Lab	Unbonded	7	3	42.6	3410
939-30B	8.08	4.00	12.56	1/5/2021	Lab	Unbonded	28	4	77.0	6130
939-30C	8.03	4.00	12.55	1/5/2021	Lab	Unbonded	28	5	77.4	6170
939-30D	8.04	3.99	12.53	1/5/2021	Lab	Unbonded	28	5	73.7	5880
939-30E		3.99	12.49	12/10/2020	Field	Unbonded	2	5	20.8	1660
939-30F		3.99	12.50	12/10/2020	Field	Unbonded	2	5	21.3	1700
939-30G		3.99	12.51	12/10/2020	Field	Unbonded	2	4	32.2	2570
939-30H				Hold	Field					
939-30I				Hold	Field					

Fracture Types

1 Cone both ends; 2 Cone one end w/ split; 3 Columnar; 4 Diagonal; 5 Side at top or bottom; 6 Pointed End

Remarks:

Reviewed By

37 Liberty Drive, Bangor, ME 04401-5874 • Tel (207) 848-6029 • Fax (207) 848-2403 • www.swcole.com

S.W.COLE ENGINEERING, INC.

Report of Concrete Compressive Strength

ASTM C-31/ C-39 / C-1231

Project Name: Hampden ME - Grist Mill Bridge - Concrete Testing

Project Number: 20-1142

Report Date: 1/5/2021

Client: T. Buck Construction, Inc.

Client Contract Number:

General Contractor:

Concrete Supplier: O.J. Folsom

PLACEMENT INFORMATION

Date Cast: 12/8/2020 **Time Cast:** 12:06 **Date Received:** 12/9/2020

Placement Location: BRIDGE DECK

Placement Method: Pump

Placement Vol. (yd³): 115

Cylinders Made By: Brendan Auth

Aggregate Size (in): 3/4

INITIAL CURING CONDITIONS

Temperatures

Minimum (°F) 52 **Maximum (°F)** 66

DELIVERY INFORMATION

Admixtures: AIR / SUPER / 2% NCA

TEST RESULTS

Slump (in) (C-143):

Air Content (%) (C-231) 8.5

Air Temp (°F): 31

Conc. Temp (°F) (C-1064): 60

Load Number: 68

Mixer Number: 3

Ticket Number 4380

Cubic Yards: 10

Design (psi): 4000

Batch 10:43

Arrive 11:30

Depart 12:00

Cylinder Designation	Cylinder Weight (lbs)	Cylinder Diameter (in)	Cross Sectional Area(In)²	Date Of Test	Cure Type	Cap Type	Age (days)	Fracture Type	Load (kips)	Strength (psi)
939-30J				Hold	Field					
939-30K				Hold	Field					

Fracture Types

Remarks:

Reviewed By

37 Liberty Drive, Bangor, ME 04401-5874 • Tel (207) 848-6029 • Fax (207) 848-2403 • www.swcole.com

S.W.COLE ENGINEERING, INC.

Report of Concrete Compressive Strength

ASTM C-31/ C-39 / C-1231

Project Name: Hampden ME - Grist Mill Bridge - Concrete Testing

Project Number: 20-1142

Report Date: 1/5/2021

Client: T. Buck Construction, Inc.

Client Contract Number:

General Contractor:

Concrete Supplier: O.J. Folsom

PLACEMENT INFORMATION

Date Cast: 12/8/2020 **Time Cast:** 2:30 **Date Received:** 12/9/2020

Placement Location: BRIDGE DECK

Placement Method: Pump **Placement Vol. (yd³):** 115

Cylinders Made By: Brendan Auth **Aggregate Size (in):** 3/4

INITIAL CURING CONDITIONS

Temperatures

Minimum (°F) 52 **Maximum (°F)** 66

DELIVERY INFORMATION

Admixtures: AIR / SUPER / 2% NCA

TEST RESULTS

Slump (in) (C-143): 6 3/4

Air Content (%) (C-231) 8.6

Air Temp (°F): 31

Conc. Temp (°F) (C-1064): 61

Load Number: 11

Mixer Number: 80

Ticket Number 4397

Cubic Yards: 10

Design (psi): 4000

Batch 1:27

Arrive 2:06

Depart 2:30

Cylinder Designation	Cylinder Weight (lbs)	Cylinder Diameter (in)	Cross Sectional Area(In)²	Date Of Test	Cure Type	Cap Type	Age (days)	Fracture Type	Load (kips)	Strength (psi)
939-31A	8.15	3.99	12.48	12/15/2020	Lab	Unbonded	7	3	49.5	3970
939-31B	8.11	3.99	12.50	1/5/2021	Lab	Unbonded	28	4	87.4	6990
939-31C	8.14	3.99	12.52	1/5/2021	Lab	Unbonded	28	3	86.3	6900
939-31D	8.17	4.00	12.53	1/5/2021	Lab	Unbonded	28	5	98.3	7840
939-31E		3.98	12.47	12/11/2020	Field	Unbonded	3	4	38.8	3110
939-31F	8.07	3.99	12.49	12/14/2020	Lab	Unbonded	6		65.8	5270
939-31G				Hold	Lab					
939-31H				Hold	Lab					
939-31I				Hold	Lab					

Fracture Types

1 Cone both ends; 2 Cone one end w/ split; 3 Columnar; 4 Diagonal; 5 Side at top or bottom; 6 Pointed End

Remarks:

Reviewed By

37 Liberty Drive, Bangor, ME 04401-5874 • Tel (207) 848-6029 • Fax (207) 848-2403 • www.swcole.com

S.W.COLE ENGINEERING, INC.

Report of Concrete Compressive Strength

ASTM C-31/ C-39 / C-1231

Project Name: Hampden ME - Grist Mill Bridge - Concrete Testing

Project Number: 20-1142

Report Date: 1/5/2021

Client: T. Buck Construction, Inc.

Client Contract Number:

General Contractor:

Concrete Supplier: O.J. Folsom

PLACEMENT INFORMATION

Date Cast: 12/8/2020 **Time Cast:** 2:30 **Date Received:** 12/9/2020

Placement Location: BRIDGE DECK

Placement Method: Pump **Placement Vol. (yd³):** 115

Cylinders Made By: Brendan Auth **Aggregate Size (in):** 3/4

INITIAL CURING CONDITIONS

Temperatures

Minimum (°F) 52 **Maximum (°F)** 66

DELIVERY INFORMATION

Admixtures: AIR / SUPER / 2% NCA

TEST RESULTS

Slump (in) (C-143): 6 3/4

Air Content (%) (C-231) 8.6

Air Temp (°F): 31

Conc. Temp (°F) (C-1064): 61

Load Number: 11

Mixer Number: 80

Ticket Number 4397

Cubic Yards: 10

Design (psi): 4000

Batch 1:27

Arrive 2:06

Depart 2:30

Cylinder Designation	Cylinder Weight (lbs)	Cylinder Diameter (in)	Cross Sectional Area(In)²	Date Of Test	Cure Type	Cap Type	Age (days)	Fracture Type	Load (kips)	Strength (psi)
939-31J				Hold	Lab					
939-31K				Hold	Lab					

Fracture Types

Remarks:

Reviewed By

37 Liberty Drive, Bangor, ME 04401-5874 • Tel (207) 848-6029 • Fax (207) 848-2403 • www.swcole.com